

68425

**SYNTHESIS AND CHARACTERIZATION OF BARIUM FERRITE POWDERS AS
RADAR ABSORBING MATERIAL**

**A THESIS SUBMITTED TO
THE GRADUATE SCHOOL OF NATURAL AND APPLIED SCIENCES
OF
THE MIDDLE EAST TECHNICAL UNIVERSITY**




**BY
ARCA İYİEL**

**IN PARTIAL FULFILLMENT OF THE REQUIREMENTS FOR THE DEGREE OF
MASTER OF SCIENCE
IN
THE DEPARTMENT OF METALLURGICAL AND MATERIALS ENGINEERING**

JANUARY 1997

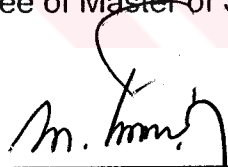
Approval of the Graduate School of Natural and Applied Sciences


Prof. Dr. Tayfur Öztürk
Director


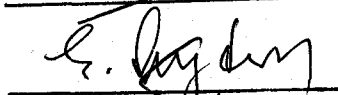



I certify that this thesis satisfies all the requirements as a thesis for the degree of Master of Science.


Prof. Dr. Mustafa Doruk
Head of Department

This is to certify that we have read this thesis and that in our opinion it is fully adequate, in scope and quality, as a thesis for the degree of Master of Science.


Prof. Dr. Muharrem Timuçin
Supervisor

Examining Committee Members

Prof. Dr. Ahmet Geveci 
Prof. Dr. Ramazan Aydın 
Prof. Dr. Muharrem Timuçin 
Doç. Dr. Ali Kalkanlı 
Doç. Dr. Abdullah Öztürk 

ABSTRACT

SYNTHESIS AND CHARACTERIZATION OF BARIUM FERRITE POWDERS AS RADAR ABSORBING MATERIAL

lyiel, Arca

M.Sc., Department of Metallurgical and Materials Engineering

Supervisor : Prof. Dr. Muharrem Timuçin

January 1997, 91 pages

Synthesis and characterization of pure and modified barium ferrite powders as radar absorbing material was the purpose of this thesis. The interaction between ferrite powder and electromagnetic waves at microwave frequencies was also studied. Submicron pure and modified with titanium and/or cobalt barium ferrite powders were prepared by the mixed oxide and chemical co-precipitation techniques. By using chemical co-precipitation technique with the aid of urea, almost monosized, homogeneous, submicron, anisotropic hexagonal platelet crystal structure as well as minimum voids RAM (Radar Absorbing Material) powders were achieved. Cobalt additions refined the powder even further when substitution level was kept at 0.5 mole CoO. Doping with titanium or with titanium and cobalt did not produce significant changes in the powder morphology. The reflection coefficients of pure and modified barium ferrites were quite low within the frequency interval 8.5 to 12.5 GHz of the microwave region.

Keywords: Barium Ferrite Powders, Radar Absorbing Material

ÖZ

RADAR SOĞURUCU MALZEME OLARAK BARYUM FERRİT TOZLARININ SENTEZİ VE KARAKTERİZASYONU

İyiel, Arca

M.Sc., Metalurji ve Malzeme Mühendisliği Bölümü

Danışman : Prof. Dr. Muharrem Timuçin

Ocak 1997, 91 sayfa

Bu tezin amacı, radar soğurucu malzeme olarak yalın ve değiştirilmiş baryum ferrit tozlarının sentezi ve karakterizasyonudur. Mikrodalga frekansında baryum ferrit ile elektromagnetik dalga etkileşimi de çalışılmıştır. Mikronaltı yalın ve titanyum ve/veya kobalt ile değiştirilmiş baryum ferrit tozları karıştırılmış oksit ve kimyasal olarak birlikte çöktürme yöntemleri ile üretilmiştir. Ure yardımıyla kimyasal birlikte çöktürme yöntemi ile neredeyse değişmez boyutlu, homojen, mikronaltı, anizotropik hegzagonal plaka kristal yapılı, minimum boşluklu radar soğurucu malzeme tozları üretimi gerçekleştirilmiştir. Kobalt miktarı 0.5 mol CoO düzeyinde tutulduğunda tozu rafine ettiği görülmüştür. Titanyum ya da titanyum ve kobalt eklenmesi toz morfolojisi açısından önemli bir değişiklik getirmemiştir. Yalın ve değiştirilmiş baryum ferritin yansıma katsayısının 8.5 - 12.5 GHz mikrodalga bölgesinde düşük olduğu gözlemlenmiştir.

Anahtar Kelimeler : Baryum Ferrit, Radar Soğurucu Malzeme

ACKNOWLEDGMENTS

I wish to thank Dr. Özlem Aydın, in the Department of Electric and Electronic Engineering at Middle East Technical University, for carrying out the measurements for electromagnetic properties of barium ferrite powder. Also I wish to thank Mr. Fatih Sayın for computing results.

Finally I wish to thank my supervisor, Prof. Dr. Muharrem Timuçin, for many helpful discussions and suggestions.

This project was financially sponsored by the Turkish Scientific and Technical Research Organization.

TABLE OF CONTENTS

ABSTRACT	iii
ÖZ	iv
ACKNOWLEDGEMENTS	v
TABLE OF CONTENTS	vi
LIST OF TABLES	viii
LIST OF FIGURES.....	ix
CHAPTER	
1. INTRODUCTION	1
2. PREVIOUS LITERATURE	6
2.1 Types of Magnetic Materials	6
2.2 Magnetic Domains	9
2.3 Crystal Structure of Barium Ferrite.....	11
2.4 Interaction With Electromagnetic Waves	13
3. EXPERIMENTAL PROCEDURE	18
3.1 General Procedure.....	18
3.2 Details	19
3.2.1 Preparation of Ferrite Powders	19
3.2.1.1 Preparation of Ferrite Powders by the Mixed Oxide Method	22
3.2.1.2 Chemical Preparation of Ferrite Powders.....	24
3.3 Powder Characterization.....	29
3.4 Determination of Dielectric and Magnetic Parameters	30
4. DATA AND RESULTS	34
4.1 Particle Characteristics of Ferrite Powders.....	34
4.1.1 Mixed Oxide Powders	34
4.1.2 Coprecipitated Powders	40

4.2	X-Ray Diffraction Data	45
4.3	Dielectric and Magnetic Measurements	62
5.	DISCUSSION AND CONCLUSIONS	85
REFERENCES	89



LIST OF TABLES

TABLES

4.1	Compositions and Morphologies of Barium Ferrite Powders Prepared by the Mixed Oxide Method.....	35
4.2	Compositions and Morphologies of Coprecipitated Barium Ferrite Powders.....	41
4.3	Diffraction Data for Pure BaFe ₁₂ O ₁₉	47
4.4	Observed Change in d-spacing of Two Major Planes.....	48
4.5	Dielectric and Magnetic Characteristics of BaFe ₁₂ O ₁₉	76
4.6	Dielectric and Magnetic Characteristics of BaFe _{11.5} Co _{0.5} O ₁₉	77
4.7	Dielectric and Magnetic Characteristics of BaFe ₁₁ CoO ₁₉	78
4.8	Dielectric and Magnetic Characteristics of BaFe _{10.5} Co _{1.5} O ₁₉	79
4.9	Dielectric and Magnetic Characteristics of BaFe _{11.5} Ti _{0.5} O ₁₉	80
4.10	Dielectric and Magnetic Characteristics of BaFe ₁₁ TiO ₁₉	81
4.11	Dielectric and Magnetic Characteristics of BaFe _{10.5} Ti _{1.5} O ₁₉	82
4.12	Dielectric and Magnetic Characteristics of BaFe ₁₁ Ti _{0.5} Co _{0.5} O ₁₉	83
4.13	Dielectric and Magnetic Characteristics of BaFe ₁₀ TiCoO ₁₉	84

LIST OF FIGURES

FIGURES

2.1	Hysteresis loops illustrating the distinction between magnetically soft and hard materials [6].....	7
2.2	Magnetic domains [9].....	10
2.3	Unit cell structure of M-hexagonal ferrite ($M^{2+}Fe_{12}O_{19}$) [6].....	12
2.4	Multi layer RAM [2].....	15
3.1	Relation of phase equilibria of the BaO:Fe ₂ O ₃ -Fe ₂ O ₃ system with hexagonal ferrites BaO:6Fe ₂ O ₃ , W, Y, Z [9].....	21
3.2	Typical flowchart for barium ferrite powder preparation.....	23
3.3	The flowchart of coprecipitation technique.....	27
3.4	Log C versus pH of each ion in aqueous solution [26].....	28
3.5	Network diagram of dielectric and magnetic properties measurement.....	33
4.1	Micrograph of Sample No: 2 (x750).....	36
4.2	Micrograph of Sample No: 2 (x4,000).....	36
4.3	Micrograph of Sample No: 2 (x6,500).....	37
4.4	Micrograph of Sample No: 3 (x750).....	37
4.5	Micrograph of Sample No: 3 (x4,000).....	38
4.6	Micrograph of Sample No: 3 (x6,500).....	38
4.7	Micrograph of Sample No: 4 (x750).....	39
4.8	Micrograph of Sample No: 4 (x4,000).....	39

4.9	Micrograph of Sample No: 5 (x10,000).....	42
4.10	Micrograph of Sample No: 5 (x15,000).....	42
4.11	Micrograph of Sample No: 6 (x10,000).....	43
4.12	Micrograph of Sample No: 8 (x7,500).....	43
4.13	Micrograph of Sample No: 12 (x2,000).....	44
4.14	Micrograph of Sample No: 12 (x15,000).....	44
4.15	XRD diagram of Sample No: 1.....	49
4.16	XRD diagram of Sample No: 5.....	50
4.17	XRD diagram of Sample No: 2.....	51
4.18	XRD diagram of Sample No: 3.....	52
4.19	XRD diagram of Sample No: 4.....	53
4.20	XRD diagram of Sample No: 9.....	54
4.21	XRD diagram of Sample No: 10.....	55
4.22	XRD diagram of Sample No: 11.....	56
4.23	XRD diagram of Sample No: 6.....	57
4.24	XRD diagram of Sample No: 7.....	58
4.25	XRD diagram of Sample No: 8.....	59
4.26	XRD diagram of Sample No: 12.....	60
4.27	XRD diagram of Sample No: 13.....	61
4.28	Absorption characteristics of Sample No: 5.....	67
4.29	Absorption characteristics of Sample No: 6.....	68
4.30	Absorption characteristics of Sample No: 7.....	69
4.31	Absorption characteristics of Sample No: 8.....	70
4.32	Absorption characteristics of Sample No: 9.....	71

4.33	Absorption characteristics of Sample No: 10.....	72
4.34	Absorption characteristics of Sample No: 11.....	73
4.35	Absorption characteristics of Sample No: 12.....	74
4.36	Absorption characteristics of Sample No: 13.....	75
5.1	Reflection loss characteristics of the ferrite powders produced in the present study as compared with the reflectance quoted in literature [3].....	88



CHAPTER I

INTRODUCTION

There is in existence today scarcely a piece of electronic equipment that does not contain ceramic magnets in one form or another. These materials came into general use in industrial applications more than a century ago, and they have been used in telephone circuits almost since the beginning of that industry. But only in recent decades have magnetic materials become universally accepted for application at higher frequencies and at very high frequencies. Very recently they have found their way to uses in new applications of microwaves.

Microwaves are electromagnetic waves of frequencies ranging between 300 MHz and 300 GHz. This places microwave in the electromagnetic spectrum of frequencies just above radio waves (Very High Frequency) used in FM and television broadcasting and just below the deep infrared. The UHF (Ultra High Frequency) range of television frequencies falls technically within the microwave range. When microwaves are used in communication, they act as a carrier wave for encoded information.

Ceramic ferrites, both hard and soft magnetic types are known to interact with electromagnetic waves. Therefore, they are used to manufacture parts like antennas, yokes and frequency filtering elements of various communication devices.

Recently, magnetic ceramics found a new area of application: They are being used to manufacture coatings which absorb microwaves. One specific application is noteworthy: [1] The outer surface of military aircraft is painted with a resin which carries ceramic magnet particles, the coating carrying these embedded particles absorb the approaching radar waves

and makes the aircraft almost immune to radar detection. This particular application, which creates low-observable aircraft, is generally referred to as "Stealth Technology".

Coatings based on Radar Absorbing Material (RAM), suck in and dissipate the electromagnetic energy of a radar wave instead of reflecting it back to its source. RAM coatings absorb radar waves by converting their electromagnetic energy into motion [2].

During the '70s and '80s, several big and small firms began to develop still lighter and more effective RAM coatings and stealthy structures. RAM was first used by submerged German submariners to hide them from Allied radar. Until the beginning of 90's the most commercially available RAM's were made of nonmagnetic materials. A new class of RAM'S made of ferrites has become commercially available since '93.

Stealth aircraft are built mostly from composites made of carbon fiber-reinforced resin, a radar absorbing structure. When a radar wave strikes the carbon, electromagnetic energy creates a current that is bled off as it heats the fiber, even infinitesimally. RAM products of some firms are either magnetic or dielectric absorbers. Magnetic absorbers consist of a rubber, polyurethane, fluoroelastomer, or silicon matrix loaded with ferrites or graphites. These bleed off radar energy by vibrating when they come in contact with the magnetic component of an electromagnetic field. They can be tuned to absorb specific frequencies or broad bands of energy by tailoring the magnetic properties of ferrites, coating thickness, loss factor, and impedance [1].

Yet some radar energy may still be reflected. At least two strategies exist to prevent those waves from being echoed back to hostile radar stations. One is to disperse the radar so it does not reflect back. This strategy is used in some aircraft whose prismatic shape rarely provides surfaces radar transmitters can recognize. The other strategy is to trap the waves inside the structure. Underneath some aircraft's smooth leading edge, its airframe zigzags like a saw. The spaces between the teeth are filled with RAM, bound on both sides by the titanium airframe. Once a radar wave enters the tapered wedge, it rebounds through the RAM from

one titanium side to the other until it runs out of energy [1]. In other words, most RAM's are designed using a lossy dielectric in the form of pyramids, mounted side by side, and connected at the base, forming a continuous slab of lossy dielectric. The reason for this design is to make a gradual transition from the wave impedance of the incident media to that of the lossy dielectric slab, minimizing the reflection of the incident wave. The RF energy that penetrates the pyramidal structure is then absorbed in the lossy dielectric slab at the base of the RAM. Most RAM designs are empirical and are considered proprietary information of RAM manufacturers [2].

Usefulness of ferrites as radar absorbers is based on certain fundamental physical, chemical, magnetic and electronic properties such as crystal structure, saturation magnetization, anisotropy energies, Curie temperature, permeability, permittivity, dielectric loss and hysteresis loop. It is the magnitude and interrelations of those properties that permit practical applications. For example, ferrites have been used for compact wideband microwave absorption particularly at microwave frequencies due to the low reflection coefficients based on their magnetic permeabilities.

The materials for magnetic ceramics are produced by powder processing techniques. For example, the soft type magnetic ceramic $MgO_xMnO_{(1-x)}Fe_2O_3$ which is used at microwave frequencies is manufactured by mixing the constituent metallic oxides in powder form, extruding or pressing these materials in the desired shape, and firing the mixture at temperatures higher than 1100 °C. Use of powders allows to make various compositional modifications easily so that, by adhering to a fixed major nominal composition ferrite magnets of widely differing characteristics can be obtained.

Amin and James [3, 4] published two papers consecutively in 1981 in the Journal of Institution of Electronic and Radio Engineers which described the use of hexagonal ferrites in the production of radar absorbing coatings. The particular ferrite was of hard magnet type with the molecular formula $BaFe_{12}O_{19}$. It was claimed [3] that, by powder processing, the basic composition could be modified to include elements

like cobalt and titanium. Such compositional alterations were stated to effect the key material properties, which are important for consideration in radar absorption. These key parameters were stated to be the complex dielectric permittivity and complex dielectric permeability.

Although Amin and James [3] incorporated curves which showed the variation of magnetic permeability characteristics with modifications of the ferrite composition they did not disclose the specific effects caused by the cobalt and titanium additions.

In 1993, J. Perini and L.S. Cohen [2] of Naval Research Laboratory in U.S.A., published a paper dealing with the optimization of RAM based on computer modelling. The radar absorbing component of the RAM composites used in their model was also magnetic ceramic powder but no compositional or morphological details were given.

The present thesis study was initiated with the aim of producing barium ferrite powders suitable for use in making radar absorbing coatings. An outstanding feature of this ceramic powder is that its morphology may be altered by variations of basic composition and the method of powder synthesis. Hence powders can be obtained acicular as needles, or as sphere like equiaxed particles, or in the form of hexagonal platelets thin like fish scale. In the present study, the goal was to obtain hexagonal platelets since these are amenable more to a planar alignment which will force them to self-orientation during painting as the RAM coat.

A further goal of the thesis was to examine the effects of cobalt and titanium additions on the crystal structure of the hexagonal ferrite and their influence on the key material parameters like the complex dielectric permittivity, ϵ , and the complex magnetic permeability, μ . The parameters were determined by establishing interaction of electromagnetic waves with powder of barium ferrite in a circuit simulated to function as a vector network analyzer. The compositions of the powders were modified by cobalt and titanium additions with the aim of ascertaining their effects on RAM properties. It should be mentioned, at the outset, that the dielectric and magnetic parameters determined with the help of the network analyzer pertain to the composite formed by the powder and the voids.

Hence the values of ϵ and μ do not represent those pertaining to the bulk of the ferrite powder examined.



CHAPTER II

PREVIOUS LITERATURE

2.1 Types of Magnetic Materials

Various types of magnetic materials are classified by their magnetic susceptibility, χ_m . Most materials are *diamagnetic* and have very small negative susceptibilities (about 10^{-6}) [5]. Examples are the inert gases, hydrogen, many metals, most non-metals and many organic compounds. In these instances the electron motions are such that they produce zero net magnetic moment. When a magnetic field is applied to a diamagnetic substance the electron motions are modified and a small net magnetization is induced in a sense opposing the applied field. As already mentioned, the effect is very small and of no practical significance in the present thesis.

Paramagnetics are those materials in which the atoms have a permanent magnetic moment arising from spinning and orbiting electrons. An applied field tends to orient the moments and so a resultant is induced in the same sense as that of the applied field. The susceptibilities are therefore positive but again small, usually in the range 10^{-3} to 10^{-6} . An important feature of many paramagnetics is that they obey Curie's law i.e. susceptibility is inversely proportional to temperature, $\chi_m \propto 1/T$, reflecting the ordering effect of the applied field opposed by the disordering effect of thermal energy. The most strongly paramagnetic substances are compounds containing transition metal or rare earth ions and ferromagnetic and ferrites above their Curie temperatures.

Ferromagnetic materials are spontaneously magnetized below a temperature termed the Curie point or Curie temperature (the two terms

are synonymous). The spontaneous magnetization is not apparent in materials which have not been exposed to an external field because of the formation of small volumes (domains) of material each having its own direction of magnetization. In their lowest energy state the domains are so arranged that their magnetizations cancel. Since the spontaneous magnetization may be several orders of magnitude greater than the applied field, ferromagnetic materials have very high permeabilities. When the applied field is removed some part of the induced domain alignment remains so that the body is now a 'magnet' in the ordinary sense of the term. The overall relation between field strength and the magnetization is the familiar hysteresis loop as shown in Figure 2.1

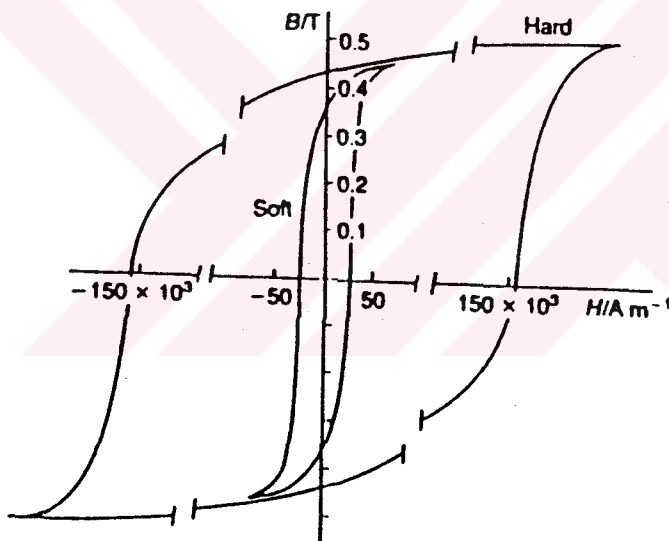


Figure 2.1 Hysteresis loops illustrating the distinction between magnetically soft and hard materials [6].

Some ceramics exhibit a permanent magnetization, termed *ferrimagnetism* which is defined as magnetism with unbalanced antiparallel magnetic alignment. From the point of view of electrical properties, these materials are semiconductors or insulators, in contrast to metallic magnetic materials which are electrical conductors. One

consequence of this is that the eddy currents produced by the alternating magnetic fields which many devices generate are limited in ferrites by their high intrinsic resistivities. To keep eddy currents to a minimum is of paramount importance as the operating frequency increases and this lead to the widespread introduction of ferrites for high frequency inductor and transformer applications [7]. Ceramic magnets have become firmly established as electrical and electronic engineering materials. Most ceramic magnets contain iron as a major constituent, therefore they are known as "ferrites" [6]. The story of ferrites began with the search for ferrimagnetic materials of unusually high resistivity to obtain reasonable eddy current losses. When a ferromagnetic material is immersed in an alternating magnetic field, eddy currents are generated in it, which dissipate energy. These losses can be reduced by lamination of the ferromagnetic core to restrict the eddy current paths, but there is a practical limit to the thinness to which laminations can be satisfactorily manufactured. However, since eddy current losses in ferromagnetic materials are inversely proportional to the resistivity, they can be minimized by use of magnetic materials of high resistivity. Indeed, this requirement of unusually high resistivity is imperative at microwave frequencies, as the eddy current power loss is proportional to the square of the frequency, for ordinary ferromagnetic materials. Ferrites, having a resistivity of up to 10^7 ohm-meter as compared to 10^{-7} ohm-meter for iron, reduce the eddy current losses in them to negligible values at microwave frequencies [6].

Ferrites with high coercivity are called *hard ferrites*. Coercivity, H_C , is a measure of the ease of demagnetization. The high coercivity of hexaferrites depends basically on their high magnetocrystalline anisotropy which results in anisotropy fields approximately 1400 kA/m. Reduction in particle size advances coercivity [8].

The important hard ferrites are the hexaferrites or M-type ferrites, characterized by the compound $MeFe_{12}O_{19}$ (Me = barium, strontium, lead) with the magnetoplumbite structure. Their hard magnetic nature is due to the large magnetocrystalline anisotropy, with the hexagonal c axis as the preferred direction. M type ferrites are widely used as permanent magnet materials.

2.2 Magnetic Domains

The spontaneous parallel alignment of magnetic moments within a crystal results in a large saturation magnetization, M_S , of the crystal. As shown in Figure 2.2a, the aligned magnetic moments also produce a large external magnetic field since the lines of magnetic force must close. There is a substantial energy associated with this external field. This energy can be reduced by closure of magnetic lines of force within the crystal. Formation of magnetic domains within the crystal eliminates the external field and thereby lowers the overall energy.

As illustrated in Figure 2.2b and 2.2c, formation of domains of opposite magnetization substantially lowers the external force lines to the ends of the crystal [9].

Domain arrangements leading to a zero external magnetic field M_S can be formed using *domains of closure*, Figure 2.2d, which make angles of 45° with respect to the magnetization in rectangular domains. Consequently, since there are no poles in the material, there is no external field associated with the magnetization and the flux is complete within the crystal. However, domains of closure are also opposed by *magnetostrictive energy*. The crystal increases in length in the direction of magnetization. Therefore, domains of closure are opposed by these elastic forces.

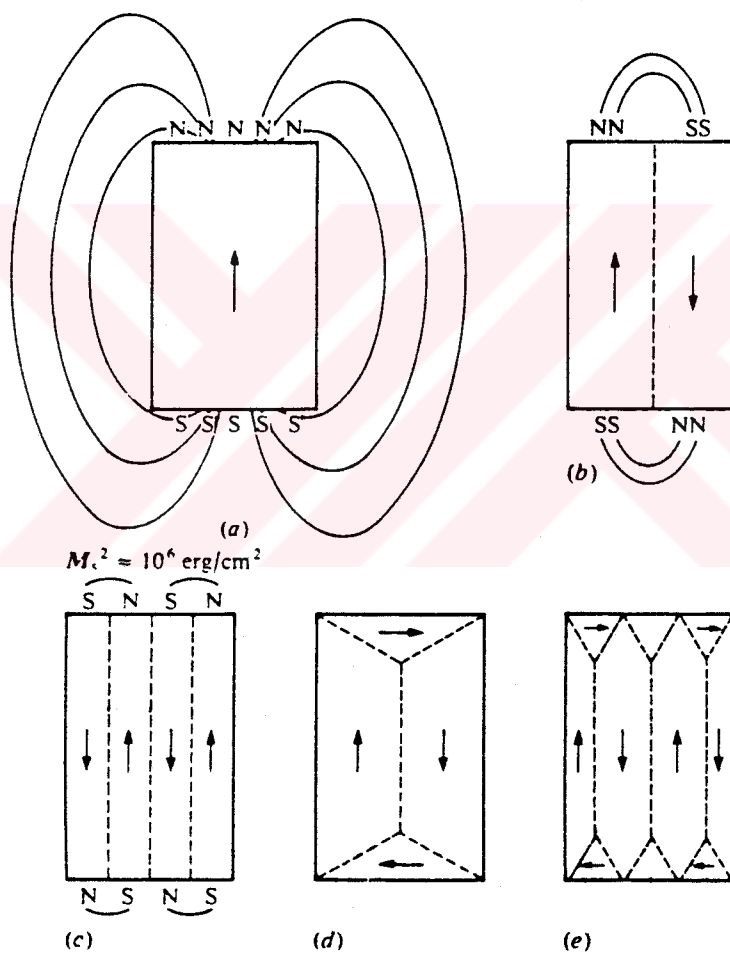


Figure 2.2 Magnetic domains [9].

The energy required for domains of closure comes from crystalline anisotropy energy. This energy tends to make the magnetization of a domain line up along certain crystal directions. These axes are known as preferred axes, or axes of easy magnetization.

In order to form domains of closure, work must be done against these elastic forces. The transition layer separating adjacent domains is called the *Bloch wall*. The exchange energy is lower for a gradual change of spin. The thickness and energy of the wall is a balance of exchange energy favouring thickness and anisotropy energy. This favours a decreasing thickness because of magnetostriction.

The width of the domains is also a balance of energy. Wall energy tends to increase domain width, anisotropy energy tends to decrease width (due to domains of closure).

The subdivision into the smaller domains, Figure 2.2e continues until the energy required for an additional domain wall is greater than the reduction in magnetic field energy [9].

2.3 Crystal Structure of Barium Ferrite

Barium ferrite is isostructural with the naturally occurring mineral magnetoplumbite, $\text{PbFe}_{7.5}\text{Mn}_{3.5}\text{Al}_{0.5}\text{Ti}_{0.5}\text{O}_{19}$ [10]. The hexagonal structure is represented in Figure 2.3 and is considerably more complex than spinel being built up of oxygen layers which have both cubic and hexagonal close packing [11]. The coordination environment of the cations is complicated and the competing magnetically opposing moments of the Fe^{3+} ions result in a saturation magnetization of nearly 4000 [12].

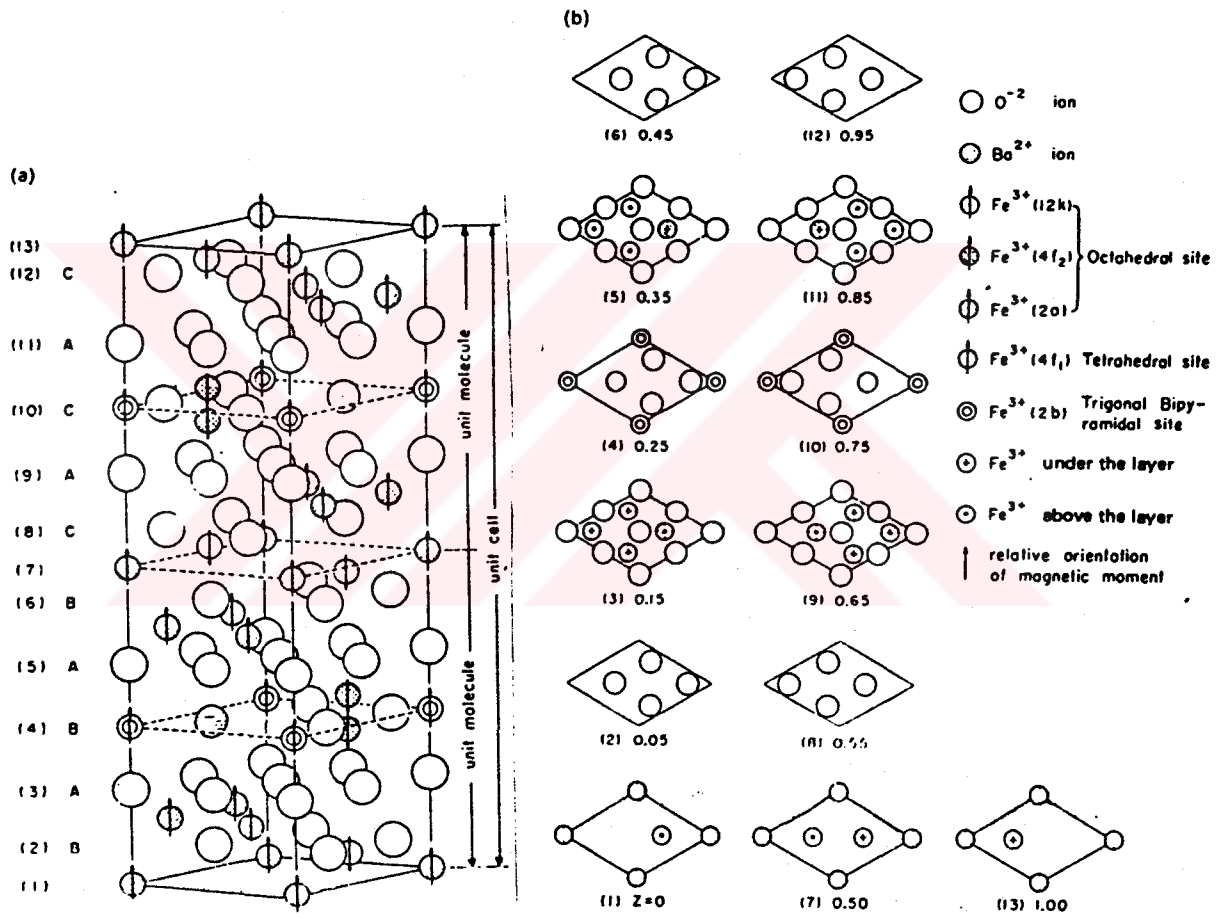


Figure 2.3 Unit cell structure of M-hexagonal ferrite ($M^{2+}Fe_{12}O_{19}$). Stacking of oxygen layers in the C (magnetically active) direction shows both cubic and hexagonal close packing [6].

The large unit cell contains two formula units with a total of 64 ions. The Ba^{2+} and O^{2-} ions together form a close-packed unit and others hexagonal close-packed. The origins of the magnetic properties are basically the same and can be summarized as follows: of the twelve Fe^{3+} ions in a formula unit, nine are on octahedral sites, two on tetrahedral sites, and one on a five-coordinated site. Seven of the ions on octahedral sites and the one on a five-coordinated site have their spins in one sense, and the remainder are oppositely directed. Thus, there are four more ions with spins in the one sense than there are with spins in each Fe^{3+} ion, there are 20 unpaired spins per formula unit, leading to a saturation magnetization of $20 M_B$ per cell volume [6]. $\text{BaFe}_{12}\text{O}_{19}$ has a high magnetic anisotropy with its easy direction along the c-axis.

2.4 Interaction With Electromagnetic Waves

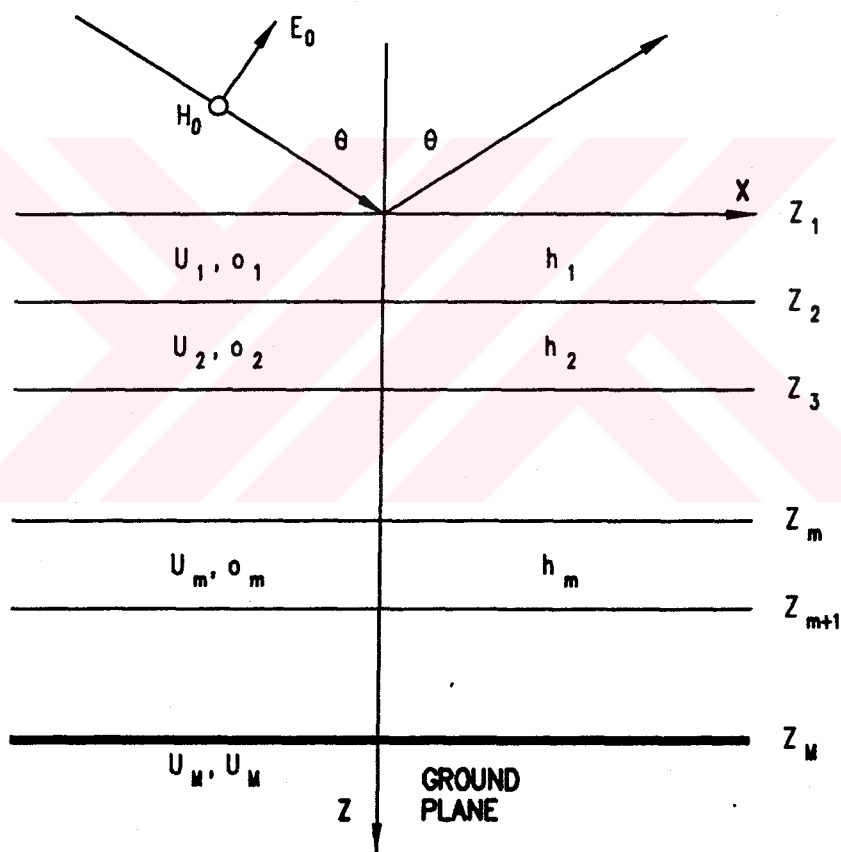
If a transverse electromagnetic wave propagates in an unmagnetized ferrite, its wavelength will be smaller than in free space because of the ferrite dielectric constant. Dielectric losses are normally small because electrical conductivity is low, whereas other losses resulting from polarization and relaxations are negligible. Ferrite permeability decreases and magnetic losses increase as operating frequencies approach ferromagnetic resonance. Since resonance is spread over a very wide band-width in an unmagnetized ferrite, it will act as a lossy dielectric through this region. Like barium ferrite, most RAM's are designed in the form of pyramids using a lossy dielectric. Kuester and Holloway [13] developed a technique to calculate the equivalent dielectric constant and conductivity of pyramidal RAM's. Hansen et. al [14-16] have also analyzed and measured the performance of such RAM's. None of these papers however addressed the design of RAM's with a specific performance in mind. Perini and Cohen [2] developed a method for design of RAM for large angle of incidence. They assumed that RAM is made of a layered structure of several dielectric materials. This structure may or may not be on top of a conducting (ground) plane. Usually, but not necessarily, only the last dielectric layer is lossy. The others are used to match the wave impedance of the incident media to that of the RAM; over the desired frequency bandwidth. Another way of looking at the performance of this type of RAM is the following: the first

layers bend the incident rays so that they always penetrate the last (absorbing) layer with normal incidence, therefore, maintaining the absorption rate nearly constant.

The problem of the multi layer RAM is illustrated in Figure 2.4. The planar layers are parallel to the (X, Y) plane, and are characterized by the thickness h_i , the dielectric constant ϵ_i , the conductivity σ_i , and the permeability μ_i . All layers are assumed to be infinite in extent.

In Figure 2.4, a RAM structure containing $M+1$ layers is illustrated. The layer zero is the incident media and layer M is either a perfect conductor or free space. In this figure, the last layer is taken as a perfect conductor (ground plane). The wave impedances Z_i at each interface between layers is the wave impedance of the layered structure including layers 1 to M . The formulation is valid for complex permittivities and permeabilities. Their imaginary parts represent losses. If they are constant with frequency, this implies that the dielectric and magnetic losses are inversely proportional to the frequency. Since this is not always the case, a conductivity term is used in the equations to take care of this problem.

The details of the modelling equations written by Perini and Cohen [2], as well as their solutions are outside the scope of this thesis. However, it should be mentioned that their model was centered on the calculation of the reflection coefficient, denoted as R , and a search was made for making it minimum. Amin and James [3, 4] approached the same problem by giving the priority to the "absorbance" of the wave by RAM. The analytical expressions existing in the two papers mentioned above are summarized in the following.



HOMOGENIOUS INFINITE LAYERS OVER GROUND PLANE (PARALELL INCIDENCE)

Figure 2.4 Multi layer RAM [2].

The reflection coefficient R due to the discontinuity at the interface between the free space and the RAM coating can be written as:

$$R = (Z_m - 1) / (Z_m + 1) \dots\dots\dots(2-1)$$

The reflection at the interface will be zero and all the incident energy will enter the RAM when R = 0 ; i.e., Z_m = 1. The impedance Z_m is defined by [3, 4] :

$$Z_m = (\mu_r / \epsilon_r)^{1/2} = (\mu'_r / \epsilon'_r)^{1/2} \frac{\{ 1 + j \tan \delta_\epsilon - j \tan \delta_\mu + \tan \delta_\mu \tan \delta_\epsilon \}^{1/2}}{\{ 1 + \tan^2 \delta_\epsilon \}^{1/2}} \dots\dots\dots(2-2)$$

The terms in this equation are as follows:

$$\mu = \mu_r \cdot \mu_0 = (\mu'_r - j\mu''_r) \cdot \mu_0 \dots\dots\dots(2-3)$$

$$\epsilon = \epsilon_r \cdot \epsilon_0 = (\epsilon'_r - j\epsilon''_r) \cdot \epsilon_0 \dots\dots\dots(2-4)$$

$$\tan \delta_\mu = \mu''_r / \mu'_r, \tan \delta_\epsilon = \epsilon''_r / \epsilon'_r \dots\dots\dots(2-5)$$

where μ_0 and ϵ_0 are the magnetic permeability and the dielectric permittivity of free space, respectively. μ is the complex magnetic permeability, μ' is its real part and μ'' is its imaginary part. Similar attributes apply to ϵ , ϵ' and ϵ'' as the dielectric permittivity. $\tan \delta_\mu$ and $\tan \delta_\epsilon$ are, respectively, the magnetic and dielectric loss tangents.

For full entrance of the incoming wave into RAM, the material parameters μ_r and ϵ_r should be very close to each other. When the wave enters the RAM structure it is desirable that a great part of it be absorbed inside RAM. This property is measured by the parameter called "attenuation constant", α , which is expressed as [3, 4] :

$$\alpha = 2\pi f \{ (\epsilon'_r \mu'_r) / 2 \}^{1/2} (\mu_0 / \epsilon_0)^{1/2} \cdot [(\tan \delta_\mu \tan \delta_\epsilon - 1) + (1 + \tan^2 \delta_\mu \tan^2 \delta_\epsilon + \tan^2 \delta_\mu + \tan^2 \delta_\epsilon)^{1/2}] \dots\dots\dots(2-6)$$

Thus, in addition to the desirable condition of $\mu_r = \varepsilon_r$, a good RAM should possess high values of $\tan\delta_\mu$ and $\tan\delta_\varepsilon$. The latter two are reasonable to expect because the conversion of microwave energy to thermal energy in the RAM occurs by the mechanism of dielectric losses.



CHAPTER III

EXPERIMENTAL PROCEDURE

3.1 General Procedure

The barium ferrite powders intended for use in radar absorption were produced by the conventional mixed oxide method and by chemical co-precipitation techniques. The raw mixed oxides and co-precipitated powders were given heat treatments at 1050 °C for various durations in order to convert them into the magneto-plumbite form. In order to examine the possible effects of cobalt and titanium on the crystal structure and on radar absorption behaviour, the oxides of these were introduced into the ferrite through aqueous solutions of their salts.

The variations caused by cobalt and/or titanium doping in the magnetoplumbite crystal lattice were examined by x-ray diffraction methods. The powder size and morphology were studied through scanning electron microscopy, SEM. The electro-magnetic properties of powders were investigated at microwave frequencies in the range 8.5 to 12.5 GHz by determining the complex dielectric constant ϵ and of the complex magnetic permeability μ in a computerized network analyzer. These determinations were based upon measurement of the complex reflection and transmission coefficients of the ferrite powder which was filled into a rectangular waveguide connected in series with the measuring electromagnetic circuit.

3.2. Details

3.2.1. Preparation of Ferrite Powders

Fine homogeneous powders are important for the fabrication of modern ceramics. The production of high-purity ceramic powders with controlled and reproducible properties requires an understanding of their preparation techniques and their effect on the chemical and physical properties of the ceramic particles. The use of precipitation process leads to powders with submicron, uniform particle size and homogeneity, resulting in ceramic products with throughout better physical and chemical properties (good phase formation, minimum voids) compared with those produced by the standard mixed oxide method. Nevertheless, the latter is of importance because of its lower cost. Therefore, in this study, barium ferrite powders were prepared applying chemical precipitation and the mixed oxide processes.

Figure 3.1 shows the phase diagram of the system BaO-Fe₂O₃ as taken from Hench and West [9]. The diagram shows that the magneto-plumbite compound BaFe₁₂O₁₉ is essentially a solid solution which can have considerable deficiency in iron oxide. At 1370 °C, for example, the plumbite compositions range from Fe₂O₃ = 5 moles at point (a) to Fe₂O₃ = 6 moles at point (b). Experience accumulated in previous studies revealed that the sintering behaviour and the morphologies of the plumbite powders depend very much on their molar Fe₂O₃ content. Sintering studies reported by Stuijts [17] from Philips Research laboratories indicated that the powders with less than 5.95 moles Fe₂O₃ exhibited considerably higher shrinkage than those containing more Fe₂O₃. Hence, low Fe₂O₃ powders became popular for making sintered permanent ceramic magnets.

The morphologies of the barium ferrite powders are affected by the Fe₂O₃ mole ratio and by certain additives. For example, Dey and Reed

[18] showed that acicular plumbite powders could be prepared with 5.5 moles of Fe_2O_3 in the molecular formula when 2 weight percent CaF_2 was incorporated as a mineralizer into the raw $\text{BaCO}_3 + \text{Fe}_2\text{O}_3$ mixture before calcination at $1050\text{ }^\circ\text{C}$. In contrast to this, equiaxed powders were obtained when no mineralizer was added. Barium ferrite powders tend to crystallize in the form of hexagonal platelets when the Fe_2O_3 content is close to or perfectly stoichiometric. Because such powders align more easily along the c axis they became preferred for the production of magnetic recording tapes and the read/write heads of high speed digital recording.

Among the morphological alternatives mentioned above, the RAM destined barium ferrite powders, which happen to be the subject of the present thesis, should have platelet geometry due to the c-axis orientation requirements. Thus, the $\text{BaO}/\text{Fe}_2\text{O}_3 = 1/6$ molar stoichiometry should be well-controlled to meet the morphological needs. Among the various powder preparation techniques reported in the literature [18-22] two popular methods were selected to prepare the powders needed in the present study; these are classified as the (i) the mixed oxide method, and (ii) the co-precipitation synthesis.

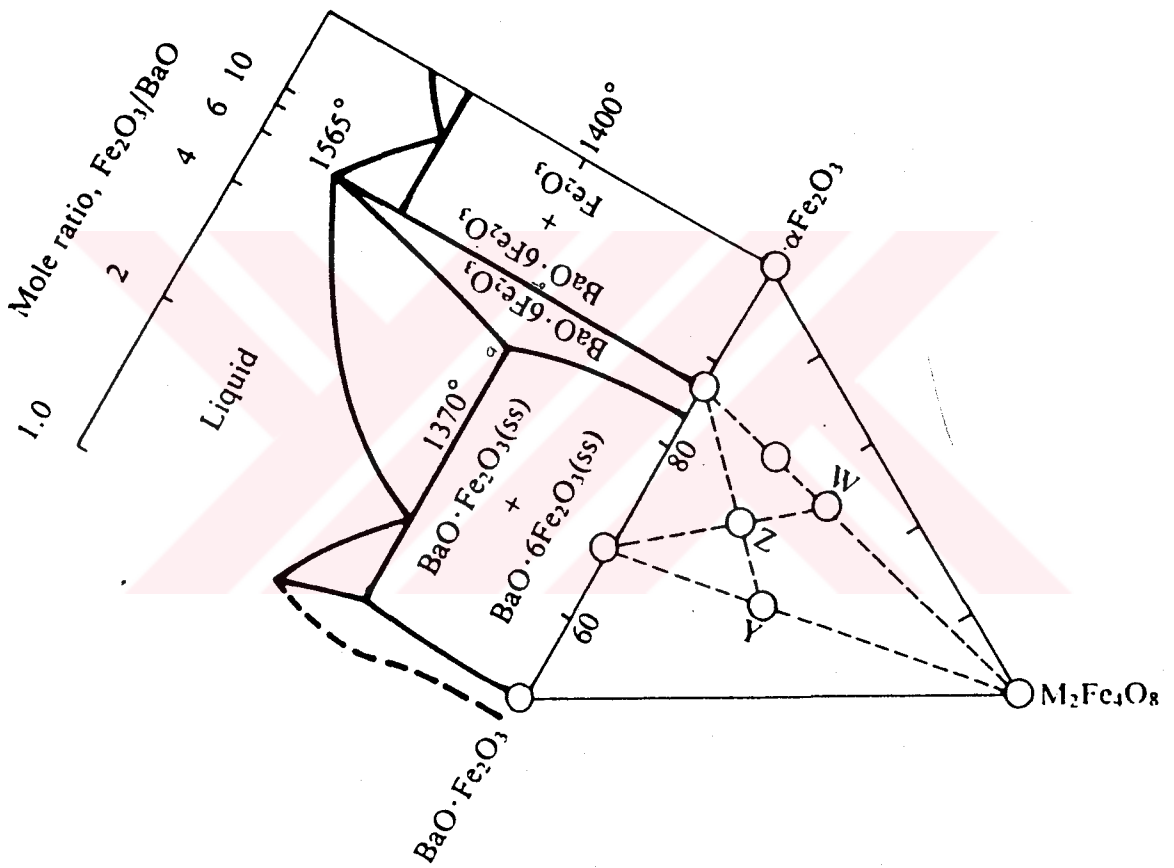


Figure 3.1 Relation of phase equilibria of the BaO:Fe₂O₃-Fe₂O₃ system with hexagonal ferrites [9] BaO : 6Fe₂O₃, W, Y, and Z where

W : BaO : 2MeO : 8Fe₂O₃

Y : 2 (BaO : MeO : 3Fe₂O₃)

Z : 3BaO : 2MeO : 12Fe₂O₃

3.2.1.1. Preparation of Ferrite Powders by the Mixed Oxide Method

The mixed oxide barium ferrite powders were prepared in accordance with the flow sheet shown in Figure 3.2. The production started with weighing BaCO_3 and Fe_2O_3 in the stoichiometric proportions of the molecular formula $\text{BaO} \cdot 6\text{Fe}_2\text{O}_3$ to yield a 20 gram batch. High purity powders of BaCO_3 (Merck 1712) and Fe_2O_3 (Merck 3924) were used as the raw materials. Titanium and cobalt substitutions in the molecular formula were made through the use of Co_3O_4 powder (Merck 2543) and TiO_2 powder (Merck 812). For purposes of thorough blending, the powders were ball milled in a covered plastic cup for 24 hours. The milling medium was distilled water and the grinding action was provided by 8 mm diameter ceramic balls made of stabilized zirconia.

The slurry obtained after milling was filtered and the filter cake was dried slowly for 12 hours in an oven at 70°C . Without any compaction, the dried cake was placed in an alumina crucible and then heated in a muffle furnace at 1010°C for 2 hours to allow the preliminary calcination reactions to occur. The reacted mass, which was cooled in the furnace to room temperature, was then ball milled for 24 hours to reduce the particle size to below 1 micron. This powder was fired for a second time at 1350°C for a duration of 5 hours. The conversion into barium ferrite was verified by x-ray diffraction analysis.

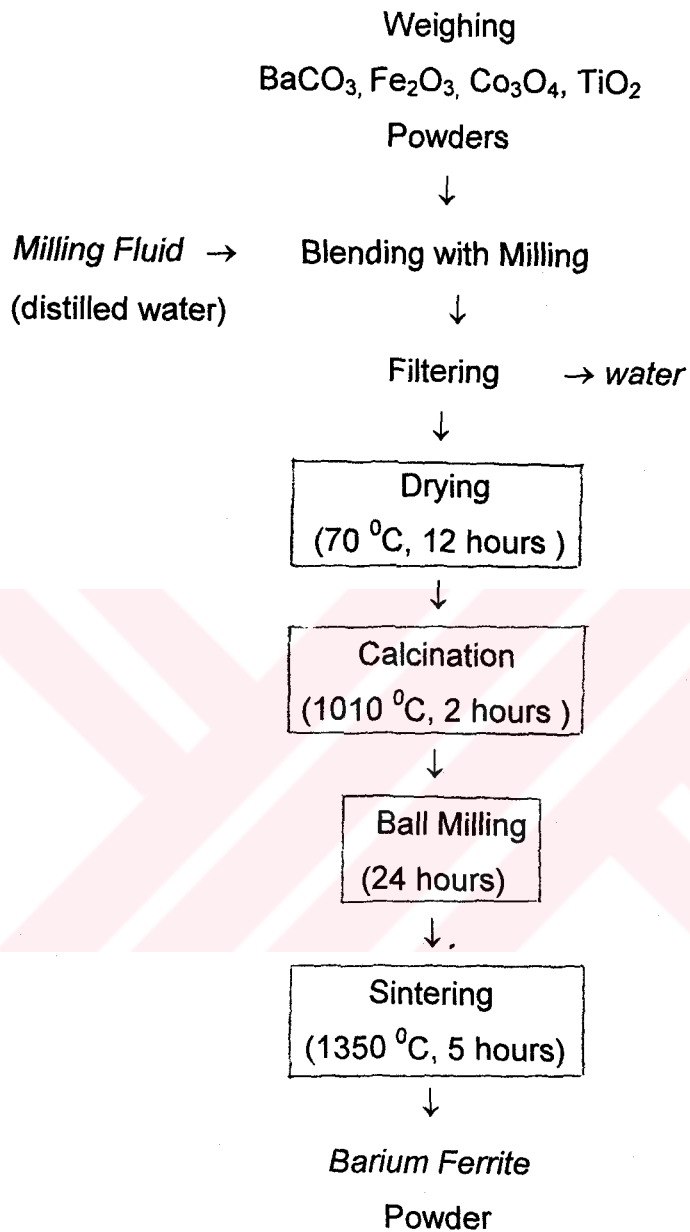


Figure 3.2 Typical flowchart for barium ferrite powder preparation.

3.2.1.2. Chemical Preparation of Ferrite Powders

Generally, the powders prepared by the mixed oxide method are rather coarse and hence must be milled for size reduction. The milling process introduces various stresses into the powder and the intrinsic coercive force, iH_c , is reduced [23-25]. This is attributed to the formation of superparamagnetic size fractions during milling. Although an annealing treatment has been advised to restore the iH_c , the annealed powder is still inferior due to the broad particle size distribution. Nevertheless, mixed oxide powders are popular because of their much lower cost as compared to those produced by chemical methods.

Preparation of ceramic powders from aqueous salt solutions became fashionable particularly in the past two decades owing to the improved properties of ceramics that can be made by their use. Chemical methods bring such advantages like chemical purity, control of stoichiometry and uniformity of particle size. In addition, the chemical processes make the doping more efficient since the dopants can be distributed more evenly, resulting in better overall chemical homogeneity.

In the present study, a co-precipitation method was used whereby hydroxides of barium and iron were precipitated simultaneously from a mixed salt solution. The precipitate acting as the chemical precursor of barium ferrite would yield, upon calcination, highly dense barium ferrite powders with micron size particles. In addition to these desirable characteristics, the particles obtained had hexagonal platelet morphology which made them ideal for RAM applications.

The aqueous salt solutions used in co-precipitation experiments were prepared from the water soluble chlorides of barium and iron. High purity $BaCl_2 \cdot 2H_2O$ (Merck 1717) and $FeCl_3 \cdot 6H_2O$ (Panreac, Montplet and Esteban SL, Spain) were the salts used in the preparation of 0.4M

aqueous solutions.

The procedure followed in a coprecipitation experiment consisted in preparing the 0.4M salt solutions and then combining these in a beaker and blending for 15 minutes on a magnetic stirrer. The volume of the chloride solutions were adjusted to obtain a 5 gram sample of barium ferrite powder in each run. The dopants titanium and cobalt were incorporated into the mixed chloride solution as their chlorides. The source of titanium was Merck 15044 TiCl_4 , and cobalt chloride was prepared in the laboratory by the action of Merck hydrochloric acid on Co_3O_4 .

The precipitating agent was an aqueous solution of NaOH and urea with or without NH_4OH . The quantities spent for one precipitation experiment were 73 grams NaOH, 93 grams urea and appropriate amount of NH_4OH to get an initial pH of 14. The reagents mentioned above were dissolved in a 2-liter capacity beaker, the solution was made up to 765 cc by distilled water additions. Prior to precipitation work, this large 2 liter beaker was placed inside a Haake water bath heated to 80 °C. The water bath was used for holding the temperature constant during the precipitation period.

The chloride solution carrying the cations was added very slowly to the beaker containing the hydroxides in a dropwise manner. The precipitation process lasted for 2 hours, during this period the contents of the beaker was stirred continuously. When the precipitation experiment ended the resulting suspension was centrifuged and washed with distilled water and finally with ethanol. The coprecipitated product was then dried in an oven at about 70 °C, followed by heat treatment at 1050 °C for 15 hours in air and cooled subsequently to room temperature.

The flowchart of ferrite production by coprecipitation technique is shown in Figure 3.3.

Coprecipitation is a chemical method of powder preparation which yields fine and homogeneous powders on atomic scale. The basic principle involved in the method is the controlled surplus of the solubility limit by achieving the supersaturation with respect to the ions present. In the coprecipitation system related to this study, the precipitating solids from the solution were hydroxides of barium and iron. The course of precipitation could be followed with reference to Figure 3.4 which shows the stability fields of the dissolved species and of the precipitates in terms of LogC and pH. LogC represents the logarithm of the molar concentration of the cation in solution. Regarding Figure 3.4, in the case of Fe-, the precipitation is complete at low pH (< 8), but Ba-hydroxide only precipitates at high pH (> 12). Therefore when the pH of the precipitating solution was below 12, some cations remained in solution, leading to the formation of other phases on heat treatment. A pH value between 12 and 13 was found to be optimum for coprecipitation of barium ferrite.

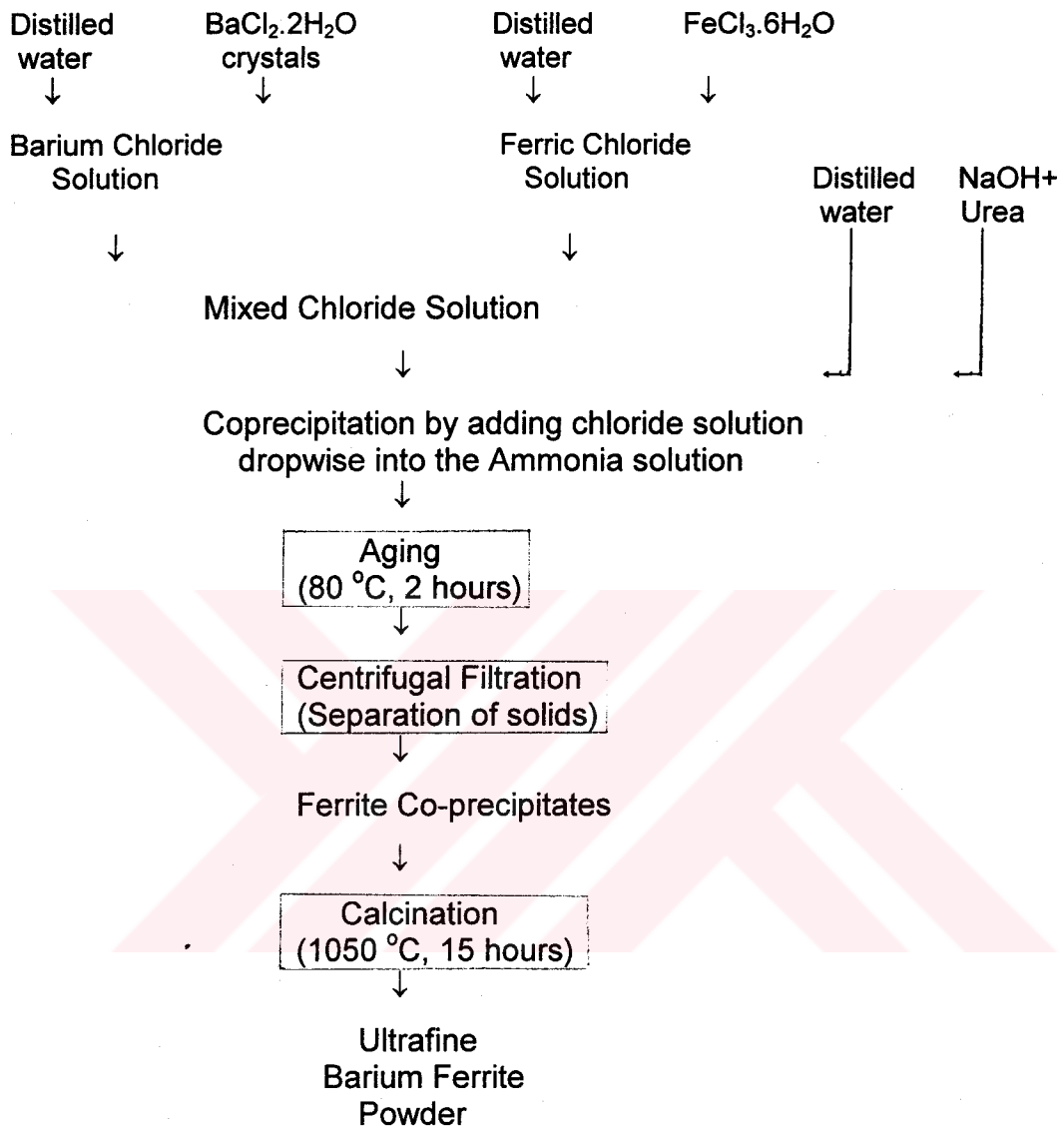


Figure 3.3 The flowchart of coprecipitation technique.

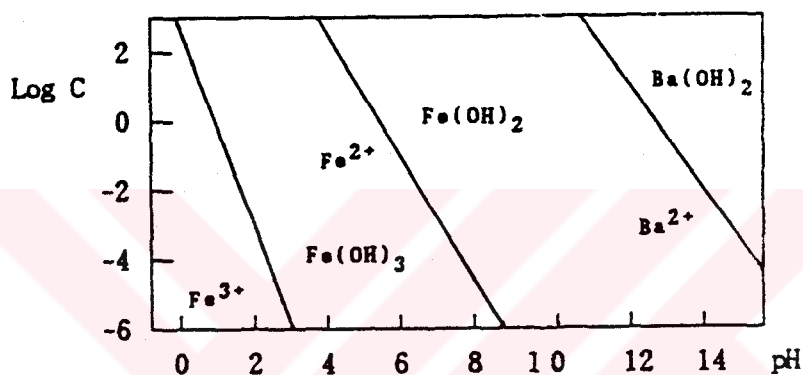


Figure 3.4 Log C versus pH of each ion in aqueous solution [26].

The action of urea, $\text{CO}(\text{NH}_2)_2$, in the precipitating medium was that on heating the solution it decomposed slowly in accordance with the following reaction:



the hydroxyl ion pumped into the solution from the decomposition of urea helped to maintain the pH of the solution stable at around 13. This caused all barium to precipitate quantitatively during the aging period.

The concentration of urea appears to effect the number of original nuclei, i.e., their number increases in the presence of a large excess of urea ($M_{\text{urea}} > 20$) resulting in smaller final particle size. The temperature of coprecipitation process, kept nearly at 85°C , was found to be critical to control the uniform growth of particles. At aging temperatures above 100°C , the rate of urea decomposition was too fast, so that secondary critical supersaturation conditions produced broad size distributions. At temperatures below 65°C , the decomposition of urea was exceedingly slow so that no substantial precipitation occurred.

3.3 Powder Characterization

The ferrite powders produced in the coprecipitation experiments were examined for their particle size, particle shape and phase purity. A JEOL 6400 Scanning Electron Microscope was used for determining the size and shape of the powder particles. Samples to be examined under the SEM were coated with gold.

Powder x-ray diffraction patterns, for phase characterization and purity determinations, were obtained from the dried precipitates, as well as for powders heat treated at 1050°C . A Rigaku D-Max/B powder diffractometer was used with a monochromate Fe K_{α} radiation at the step size of 0.04° and the count time of 1 second for phase characterization purposes. The further details of x-ray diffraction practices are depicted in Table I.

The effects of titanium and cobalt doping on the crystal lattice were examined by determining quantitatively the change in the d-spacing, calculated from the shift in the 2θ diffraction angles of the 107 and 114 planes.

3.4. Determination of Dielectric and Magnetic Parameters

The response of RAM against radar detection is influenced greatly by the complex dielectric permittivity and complex magnetic permeability of the ferrite used as RAM. The values of these parameters depend very much on the frequency of the electromagnetic wave with which the material is interacting. In the present study, the complex dielectric permittivity and complex permeability were determined at microwave frequencies with the aid of an HP X8747A Transmission-Reflection Test Unit. This unit has been housed in the Microwave and Radar Laboratory of the Electrical and Electronic Engineering Department of METU and essentially consisted of a network of waveguides into which electromagnetic waves of known frequencies were supplied from an HP 83640A Series Synthesized Sweeper signal source.

The block diagram given in Figure 3.5 shows that the wave generated by the signal source passes through the waveguide (a) and splits into two equal parts at (a); one part enters the arm (b) and the other part enters the arm (c). The arm (b) is called the "short" where the incoming wave is reflected totally at the wall and then enters the path L_1 . The other part, going into the waveguide (c), impinges upon the sample placed at the end of the waveguide. The wave interacts here with the sample, and the part which is reflected follows the path L_2 . The "Elliot" Magic Tee in the block diagram collects the two reflected waves coming from the paths L_1 and L_2 , and feeds the combined wave into the HP 70000 Spectrum Analyzer system.

The circuit shown by the block diagram in Figure 3.5 functioned like a vector network analyzer. The HP "phase shifter" X885A on the waveguide was used to adjust the difference of phase angles between the input reference signal and the combined output wave to 180° . The attenuator HP X382A, placed on the L_2 path, was adjusted until the

signals coming from L_1 and L_2 nullified each other at the magic tee; this was observed by the Spectrum Analyzer. These two adjustments gave the phase angle and the attenuation of the wave exiting from the sample side.

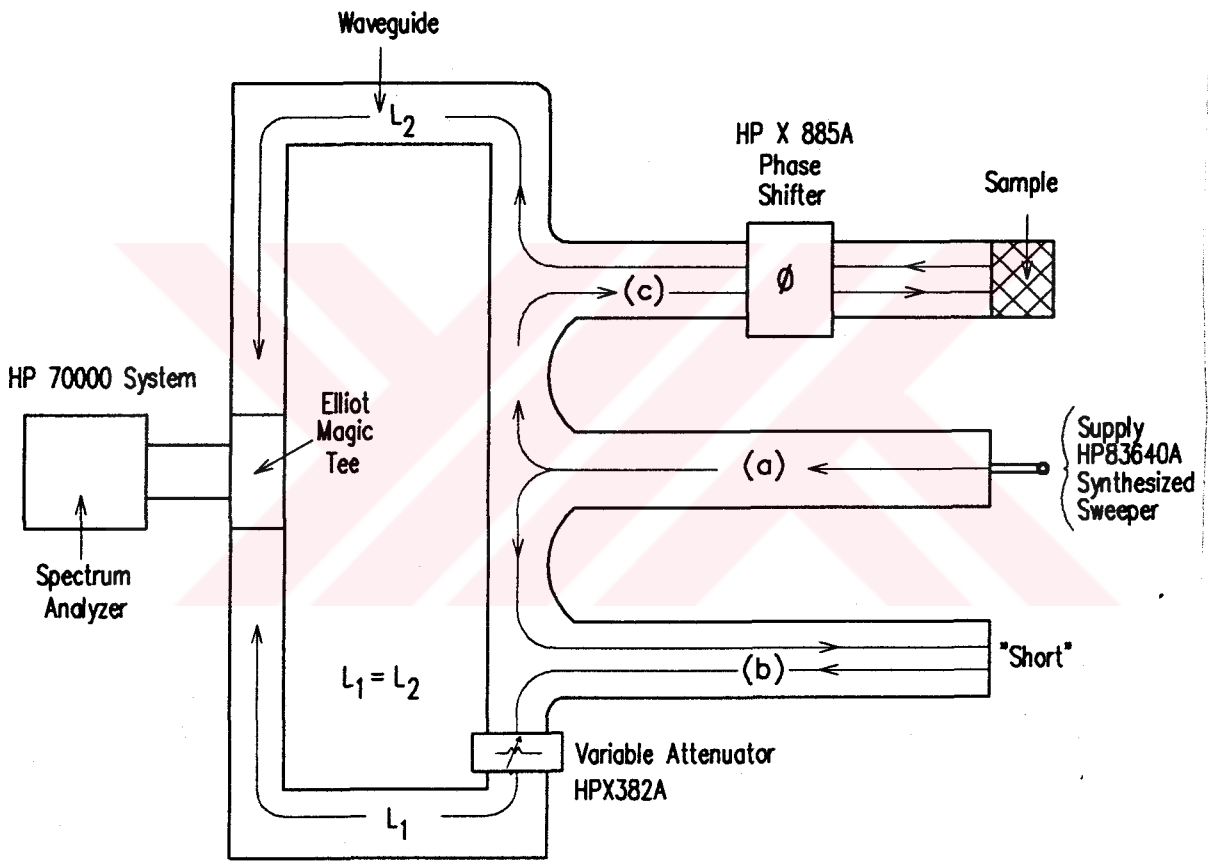
In the present study, the circuit shown in Figure 3.5 was used to measure the reflected and transmitted parts of the wave on the sample side of the system. For this purpose, the ferrite sample was placed in the cavity of the rectangular waveguide at (c). The sample cavity size was $10.16 \times 22.86 \text{ mm}^2$ in area with 3.4 mm thickness. The reflectance was measured by connecting the matched load to the end of the waveguide behind the sample and adjusting the attenuator until the reference and the output signals cancelled each other. At this point, the value read on the attenuator gave the "reflection coefficient" designated as S_{11} . For the measurement of transmittance, the match load was removed and the shorting piece was mounted to the end of the waveguide. The same procedure for obtaining null signal at the Spectrum Analyzer was repeated; the coefficient measured this time would represent a combined effect of reflectance and transmittance designated by the symbol Ψ . The transmission coefficient, indicated by S_{21} , could be calculated from Ψ and S_{11} by means of the following relationship:

$$\Psi = S_{11} - \{ (S_{21})^2 / (1 + S_{11}) \}$$

Before measurements, the entire system was calibrated by following the null procedure described above without any ferrite sample in the waveguide (c). The calibration was necessary to eliminate the reflections at connections of the circuit. The impedance of free space is known as 120π , whereas the equipment gave nearly 300. Therefore, the accuracy of the data obtained was about 20 percent.

The measurements in the network analyzer described above were confined to the frequency range of 8.5 to 12.5 GHz. This limitation was brought by the capacities of the phase shifter and of the variable attenuator and by the dimensions of the waveguide.





HP X8747A Transmission-Reflection Test Unit

Figure 3.5 Network diagram of dielectric and magnetic properties measurement

CHAPTER IV

DATA and RESULTS

4.1 Particle Characteristics of Ferrite Powders

Barium ferrite powders, synthesized as pure $\text{BaFe}_{12}\text{O}_{19}$ or doped with cobalt and/or titanium, were characterized for their particle shape and size by scanning electron microscopy, SEM. The results of these observations are summarized in the following.

4.1.1 Mixed Oxide Powders

The compositions of the ferrite powders prepared by the mixed oxide method are given in Table 4.1. In order to understand whether the platelet morphology would persist at sintering temperatures, the doped powders were pressed into 10 mm diameter and 2 mm thick discs and then fired at 1350 °C for 5 hours. The fracture surfaces of the sintered samples as observed under SEM are shown in Figures 4.1 to 4.8. These figures revealed that all doped ferrite compositions had 0.5 μm thick hexagonal platelets approximately 5 μm in diagonal. The SEM examination of the unsintered pure $\text{BaFe}_{12}\text{O}_{19}$ showed that the powder consisted of hexagonal platelets which had 3 μm diagonals and about 0.5 μm thickness.

Table 4.1 Compositions and Morphologies of Barium Ferrite Powders Prepared by the Mixed Oxide Method

Sample No	Molecular Formula of the Powder	Doping Agent(s) * and Doping Level(s)	Particle Shape and Particle Size
1	BaFe ₁₂ O ₁₉	None	Hexagonal, ** ~3 μm dia., ~3/5 μm thick
2	BaFe ₁₁ Co _{0.5} Ti _{0.5} O ₁₉	CoO=0.5, TiO ₂ =0.5	Hexagonal Plates, † ~5 μm dia, ~0.5 μm thick
3	BaFe ₁₀ Co _{1.0} Ti _{1.0} O ₁₉	CoO=1.0, TiO ₂ =1.0	Hexagonal Plates, † ~5 μm dia, ~0.5 μm thick
4	BaFe ₉ Co _{1.5} Ti _{1.5} O ₁₉	CoO=1.5, TiO ₂ =1.5	Hexagonal Plates, † ~5 μm dia, ~0.5 μm thick

* Dopant quantities are given as moles of dopant in one mole of the ferrite.

** As calcined powder

† Measured in samples sintered at 1350 °C for 5 hours.

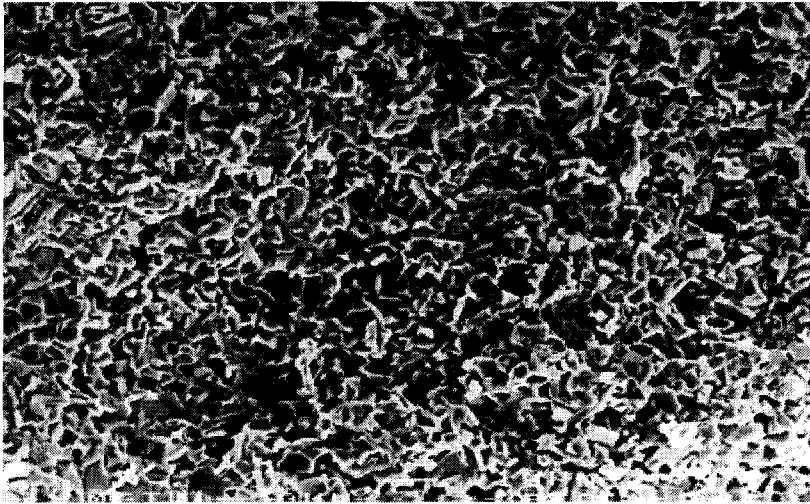


Figure 4.1 BaFe₁₁Co_{0.5}Ti_{0.5}O₁₉, prepared by mixed oxide method (x750)

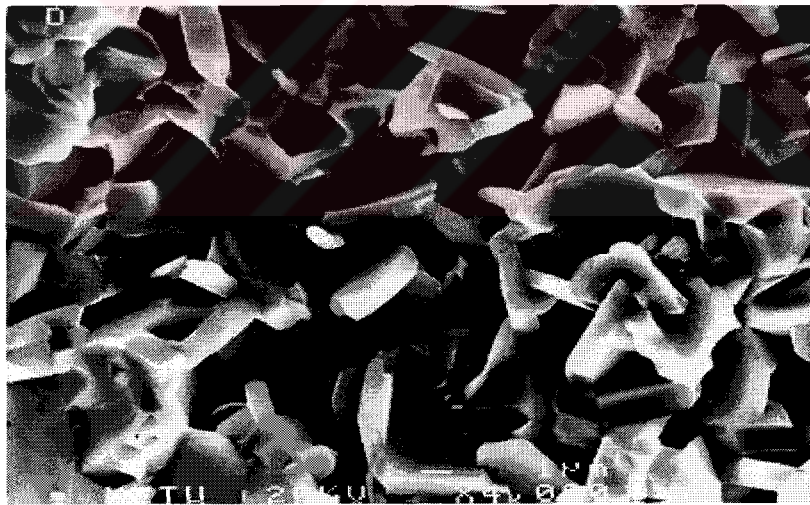


Figure 4.2 BaFe₁₁Co_{0.5}Ti_{0.5}O₁₉, prepared by mixed oxide method (x4,000)



Figure 4.3 BaFe₁₁Co_{0.5}Ti_{0.5}O₁₉, prepared by mixed oxide method (x6,500)

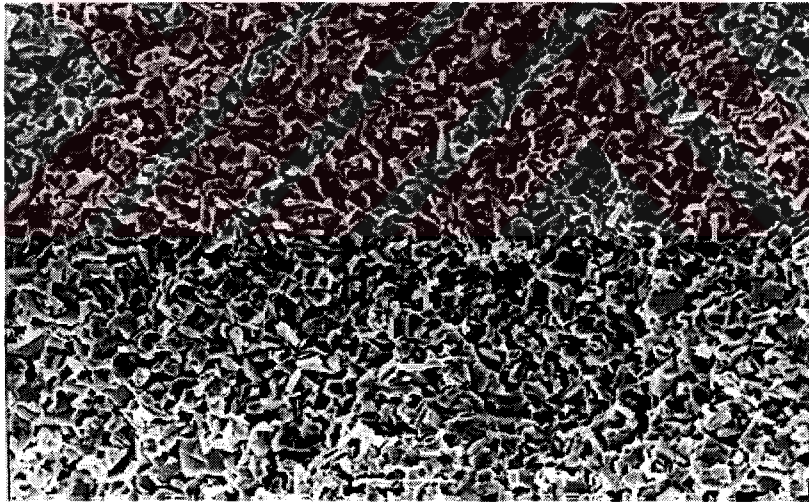


Figure 4.4 BaFe₁₀CoTiO₁₉, prepared by mixed oxide method (x750)

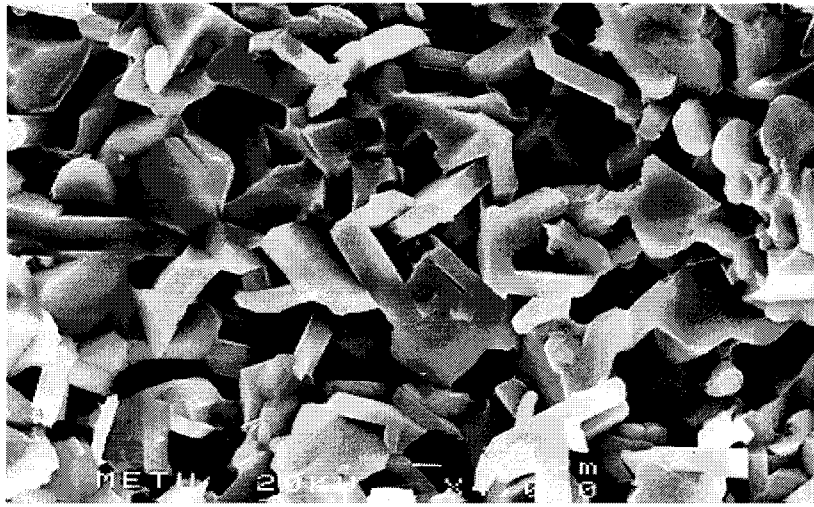


Figure 4.5 BaFe₁₀CoTiO₁₉, prepared by mixed oxide method (x4,000)



Figure 4.6 BaFe₁₀CoTiO₁₉, prepared by mixed oxide method (x6,500)

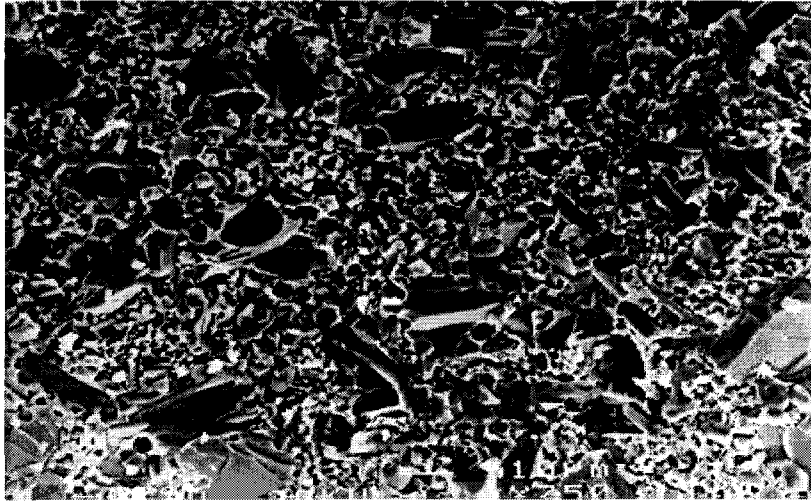


Figure 4.7 BaFe₉Co_{1.5}Ti_{1.5}O₁₉, prepared by mixed oxide method (x750)

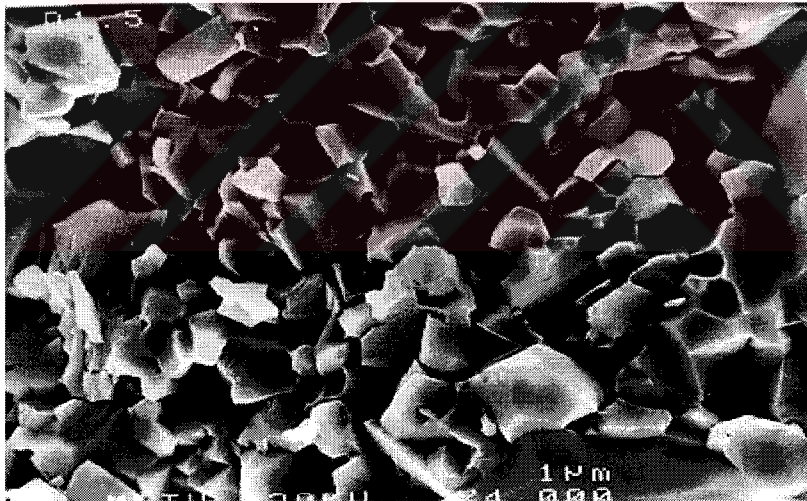


Figure 4.8 BaFe₉Co_{1.5}Ti_{1.5}O₁₉, prepared by mixed oxide method (x4,000)

4.1.2 Coprecipitated Powders

The powders produced by the coprecipitation method were examined under SEM without subjecting them to any sintering treatment. The compositions of the powders prepared are given in Table 4.2. In all coprecipitated powders, the particles had well defined hexagonal morphology. Figures 4.9 and 4.10 show the SEM micrographs of the pure $\text{BaFe}_{12}\text{O}_{19}$ powder at two different magnifications. The average size of the platelets, measured from Figure 4.10, is $0.70 \mu\text{m}$; the thickness being approximately 1/10 th of the diagonal.

Doping the ferrite with 0.5 mole cobalt oxide resulted in a dramatic decrease in the size of the hexagonal platelets. For this powder the diagonals in Figure 4.11 were estimated to be smaller than $0.2 \mu\text{m}$. Increases in the cobalt doping yielded larger platelets; as could be seen in Figure 4.12 the diagonals expanded to larger than $1.0 \mu\text{m}$.

Doping of barium ferrite with titanium alone or simultaneous doping with cobalt and titanium gave hexagonal platelet morphology which had features similar to the pure ferrite powder. Figures 4.13 and 4.14 show that the platelets of the co-doped ferrite were about $0.8 - 1.0 \mu\text{m}$ in size with approximately $0.1 \mu\text{m}$ thickness.

Table 4.2 Compositions and Morphologies of Coprecipitated Barium Ferrite Powders

Sample No	Molecular Formula of the Powder	Doping Agent(s) * and Doping Level(s)	Particle Shape and Particle Size
5	BaFe ₁₂ O ₁₉	None	Hexagonal platelet, ~ 0.7 μm dia., ~ 0.07 μm thick
6	BaFe _{11.5} Co _{0.5} O ₁₉	CoO=0.5	Very very fine, ~ 1/4 μm dia.
7	BaFe ₁₁ Co _{1.0} O ₁₉	CoO=1.0	
8	BaFe _{10.5} Co _{1.5} O ₁₉	CoO=1.5	~ 2-3 μm dia, ~ 1/5 μm thick
9	BaFe _{11.5} Ti _{0.5} O ₁₉	TiO ₂ =0.5	
10	BaFe ₁₁ Ti _{1.0} O ₁₉	TiO ₂ =1.0	
11	BaFe _{10.5} Ti _{1.5} O ₁₉	TiO ₂ =1.5	
12	BaFe ₉ Co _{0.5} Ti _{0.5} O ₁₉	CoO=0.5, TiO ₂ =0.5	~ 1 μm in dia.
13	BaFe ₉ Co _{1.0} Ti _{1.0} O ₁₉	CoO=1.0, TiO ₂ =1.0	~ 0.8 μm dia., < 0.1 μm thick

* Dopant quantities are given as moles of dopant in one mole of the ferrite.

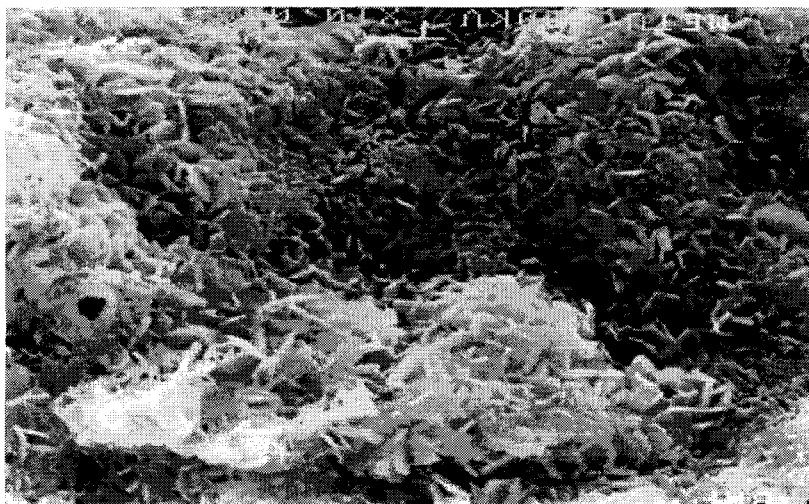


Figure 4.9 BaFe₁₂O₁₉, prepared by coprecipitation method (x10,000)

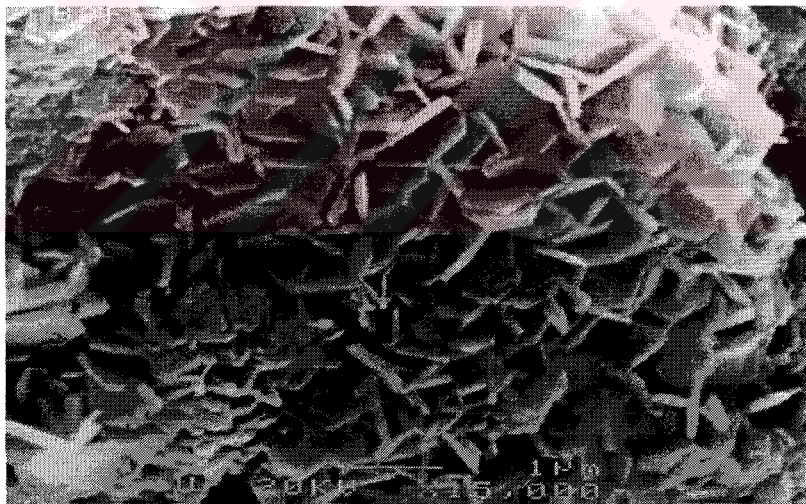


Figure 4.10 BaFe₁₂O₁₉, prepared by coprecipitation method (x15,000)

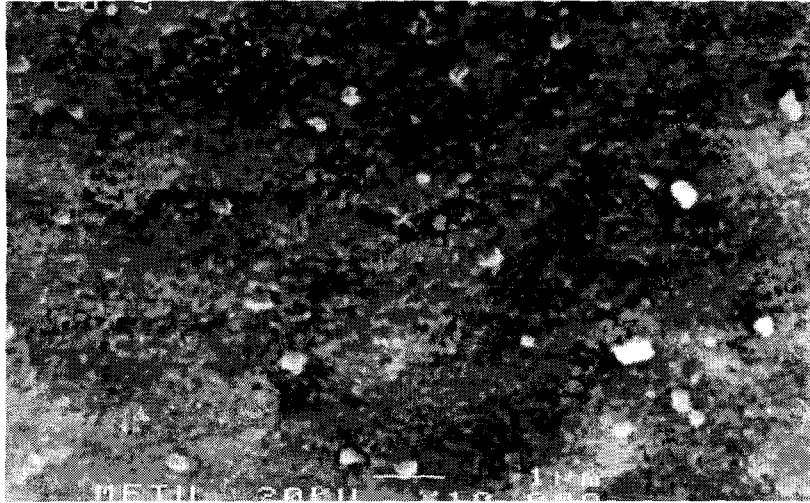


Figure 4.11 BaFe_{11.5}Co_{0.5}O₁₉, prepared by coprecipitation method (x10,000)

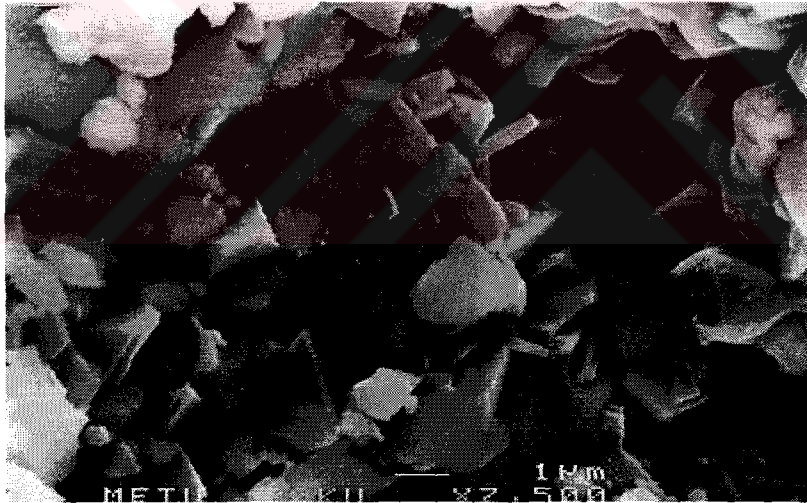


Figure 4.12 BaFe_{10.5}Co_{1.5}O₁₉, prepared by coprecipitation method (x7,500)

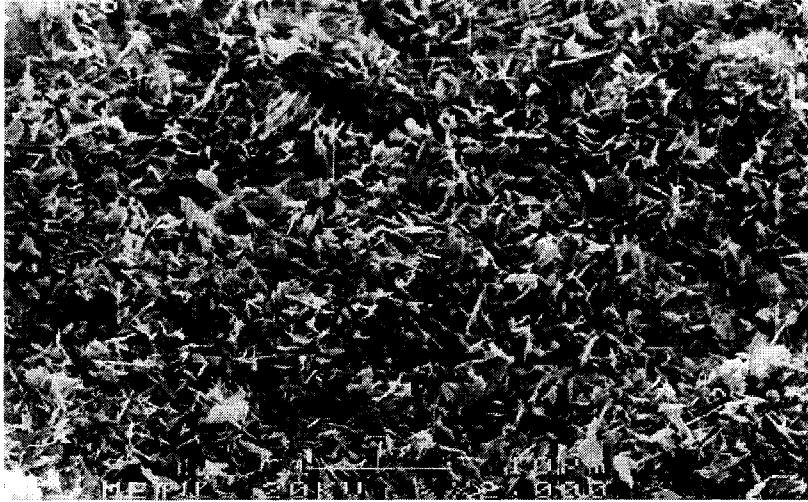


Figure 4.13 BaFe₁₁Co_{0.5}Ti_{0.5}O₁₉, prepared by coprecipitation method (x2,000)

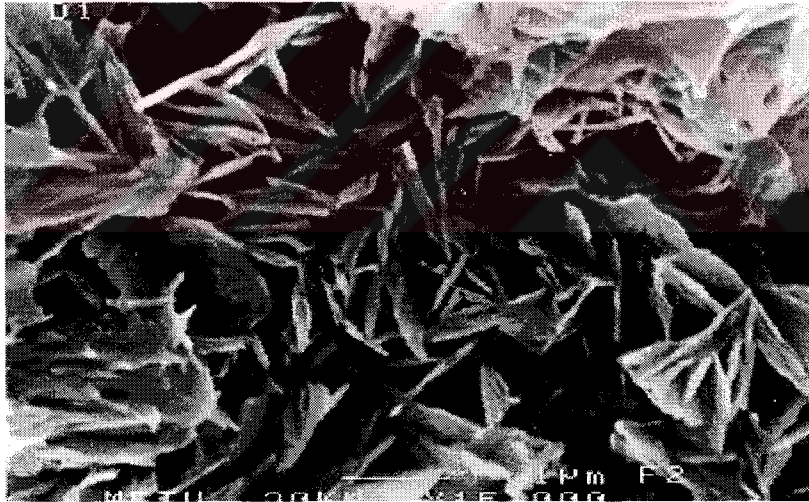


Figure 4.14 BaFe₁₀Co_{0.5}Ti_{0.5}O₁₉, prepared by coprecipitation method (x15,000)

4.2 X-Ray Diffraction Data

X-Ray diffraction charts of the pure $\text{BaFe}_{12}\text{O}_{19}$, prepared by the mixed oxide and by the chemical techniques are shown in Figures 4.15 and 4.16, respectively.

The charts contain essentially the same features, i.e the positions of 2θ angles and the relative intensities of corresponding peaks are almost identical. The diffraction data contained in the figures are transferred to Table 4.3 where the information from JCPDS are included for purposes of comparison. The comparison with JCPDS reveals that the barium ferrite powder synthesized by two different techniques in this work represent adequate crystallization.

Figures 4.17 to 4.19 show the XRD diagrams for the co-doped powders prepared by the mixed oxide process. In the pure barium ferrite the diffraction from the 200 plane of the crystal was very weak. In contrast, Figure 4.17 shows that when the barium ferrite was doped by 0.5 mole each of CoO and TiO_2 the diffraction from this plane became significant. This indicates that interaction of the 200 plane with electromagnetic radiation was enhanced by doping the material with cobalt and titanium. The same situation was observed for the peak at $2\theta=42$. Figure 4.18 and 4.19 revealed that when the doping level of cobalt and titanium increased the intensity of the peak on $2\theta=42$ decreased.

In order to understand the individual effects of titanium and cobalt on the formation of these unexpected diffraction planes the diffraction pattern of the coprecipitated ferrite powders doped singly either with titanium or with cobalt were produced. Figures 4.20, 4.21 and 4.22 show the XRD charts of barium ferrite doped with 0.5, 1.0 and 1.5 mole of TiO_2 . Comparison of these charts with that of pure $\text{BaFe}_{12}\text{O}_{19}$ indicated that TiO_2 had negligible effect on the position of the peaks, and on their intensities. On

the other hand single cobalt additions contributed largely to the formation of $2\theta=42$ and $2\theta=45$ peaks. For example, the peak at $2\theta=45$ came out intensely when 0.5 mole CoO was doped to the other part of barium ferrite as seen in Figure 4.23. This effect became pronounced with increasing the level of cobalt addition, to the extent that the diffractions from the 200 plane outweighed the diffractions from others significantly. Figures 4.24 and 4.25 show the XRD charts of barium ferrite doped with 1.0 and 1.5 mole of CoO respectively.

Figures 4.26 and 4.27 show the XRD charts of chemical process ferrite powders co-doped with titanium and cobalt. Figure 4.26 indicates that the powder produced contained numerous crystallographic planes which interacted evenly with the electromagnetic radiation.

It is observed that, the diffraction of the (114) plane shifted to higher 2θ values upon increasing substitution by cobalt oxide. This would lead to a denser packing of the atoms in the crystal. For example, the ratio of the interplanar spacing $(d_{114})_{\text{pure}} / (d_{114})_{\text{doped}}$ of the ferrite powder for CoO = 0.5 mole replacement have 0.96; indicating that atomic packing was more efficient in the presence of cobalt .

Table 4.3 Diffraction Data for pure BaFe₁₂O₁₉.

JCPDS No: 39-1433, BaFe ₁₂ O ₁₉				Sample No: 5, BaFe ₁₂ O ₁₉	
Cu K α Radiation				Fe K α Radiation	
I/I ₀	d-space, Å	2 θ	h k l	I/I ₀	2 θ
100	2,782	32,1489	1 0 7	80	40,658
98	2,628	34,0887	1 1 4	100	43,171
63	1,4738	63,0219	2 2 0	46	82,112
60	2,425	37,0416	2 0 3	50	47,023
58	1,6265	56,5355	2 0 11	42	73,001
55	2,948	30,294	1 1 0	60	38,281
53	1,6681	55,004	2 1 7	36	70,963
32	2,901	30,797	0 0 8	25	38,868
30	1,6329	56,294	3 0 4		
29	2,237	40,2835	2 0 5	42	51,236
18	2,131	42,381	2 0 6	28	53,990

Table 4.4 Observed change in d-spacing of two major planes

Sample No	Molecular Formula of the Powder	$(d_{107})_{\text{doped}}/(d_{107})_{\text{pure}}$	$(d_{114})_{\text{doped}}/(d_{114})_{\text{pure}}$
5	BaFe ₁₂ O ₁₉	1.000	1.000
6	BaFe _{11.5} Co _{0.5} O ₁₉	0.998	0.996
7	BaFe ₁₁ Co _{1.0} O ₁₉	1.004	0.963
8	BaFe _{10.5} Co _{1.5} O ₁₉	0.905	1.846
9	BaFe _{11.5} Ti _{0.5} O ₁₉	1.000	1.000
10	BaFe ₁₁ Ti _{1.0} O ₁₉	1.000	1.002
11	BaFe _{10.5} Ti _{1.5} O ₁₉	1.002	1.003
12	BaFe ₉ Co _{0.5} Ti _{0.5} O ₁₉	1.000	0.999
13	BaFe ₉ Co _{1.0} Ti _{1.0} O ₁₉	1.000	1.000

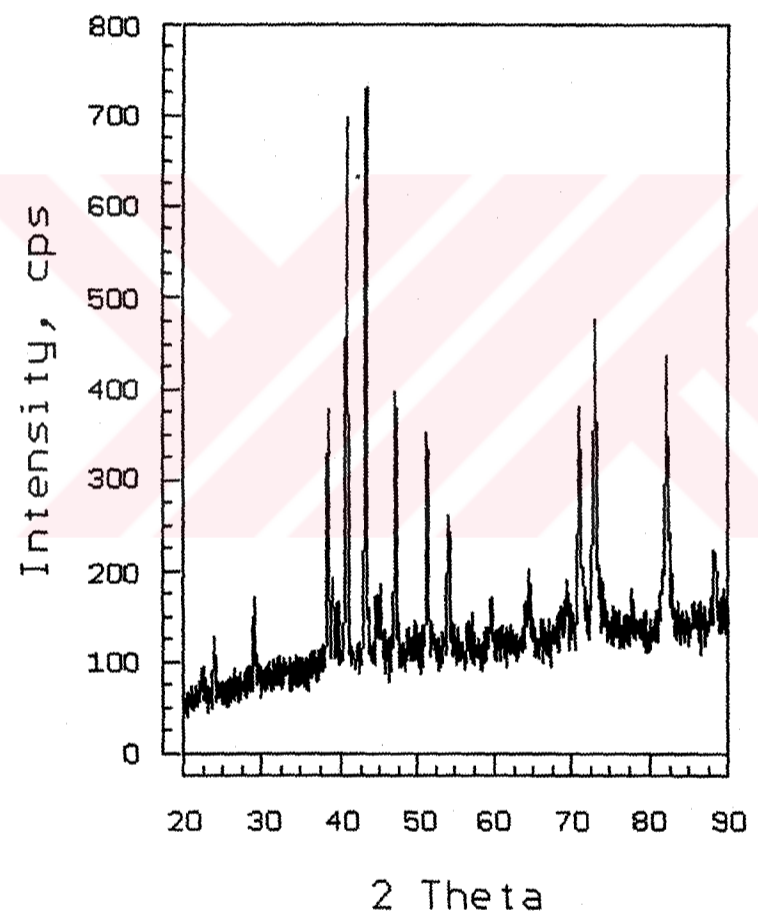


Figure 4.15. XRD diagram of pure barium ferrite, prepared by mixed oxide method.

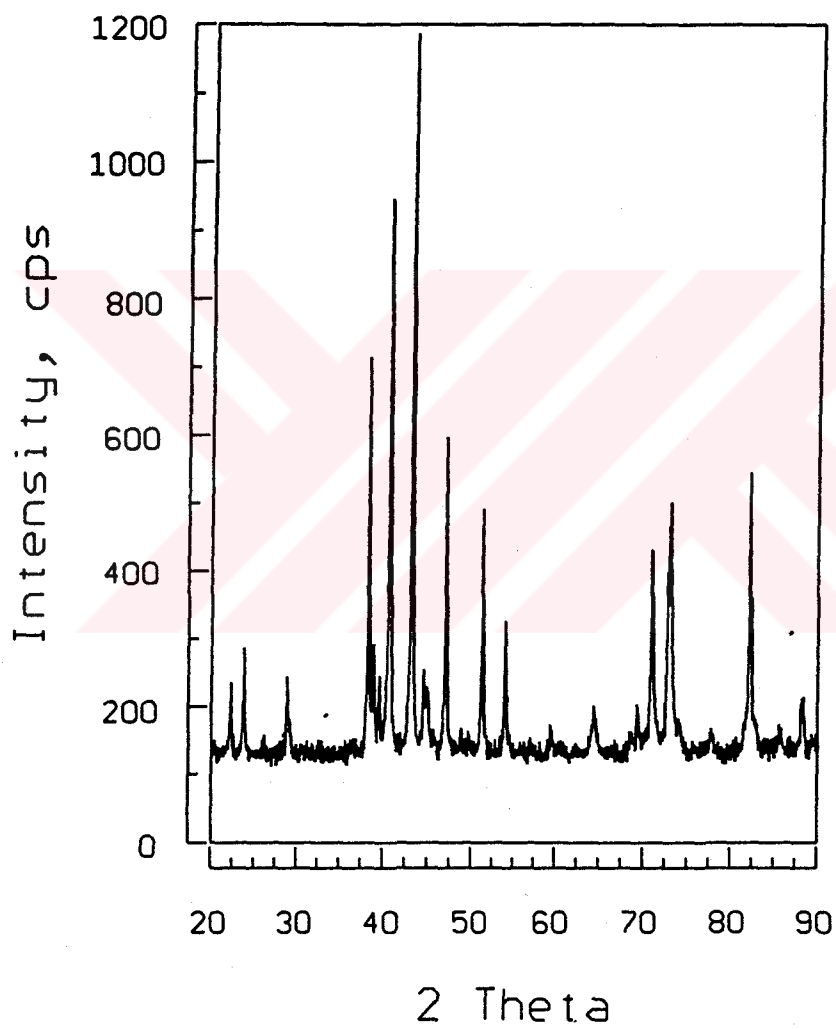


Figure 4.16. XRD diagram of pure barium ferrite, prepared by chemical precipitation technique.

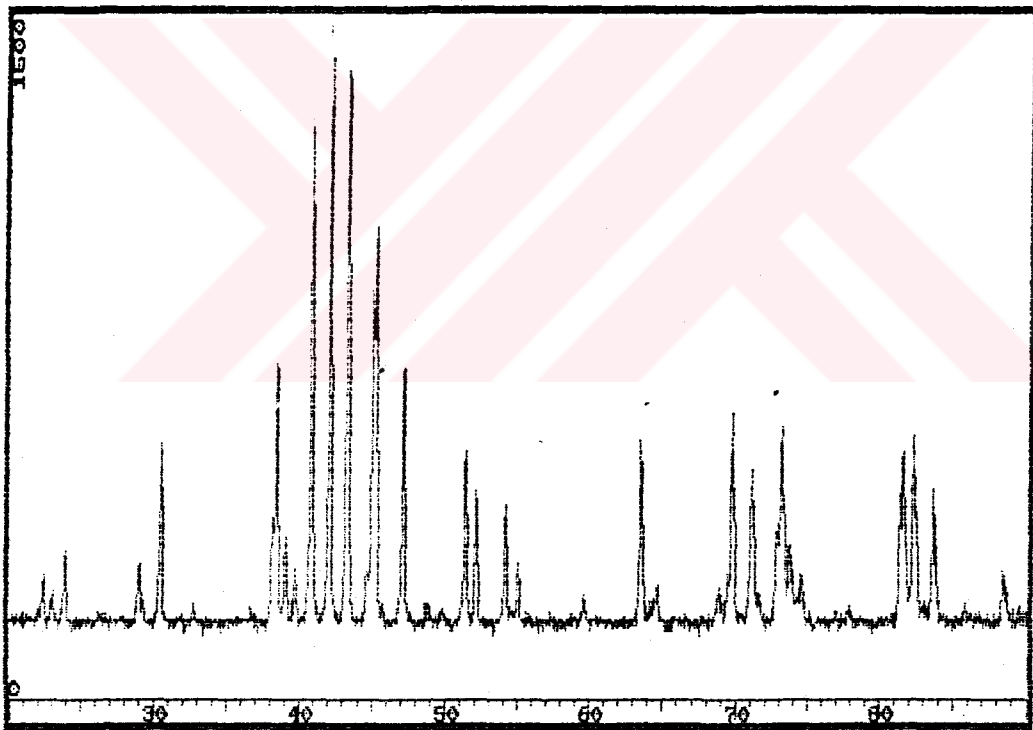


Figure 4.17. XRD diagram of $\text{BaFe}_{11}\text{Ti}_{0.5}\text{Co}_{0.5}\text{O}_{19}$ prepared by mixed oxide method

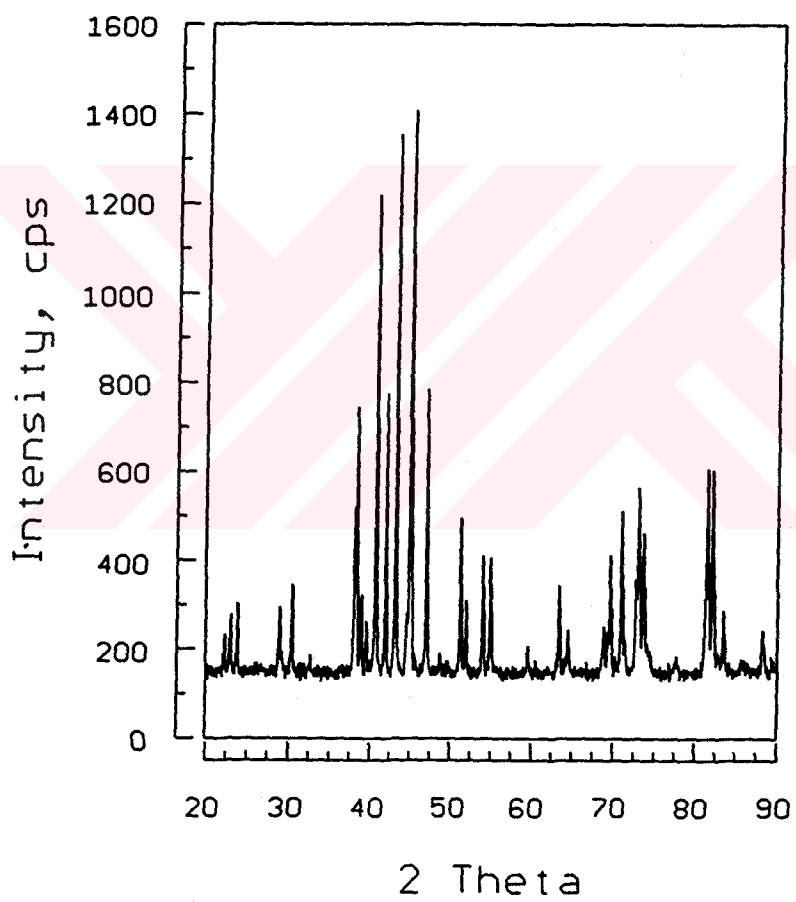


Figure 4.18. XRD diagram of $\text{BaFe}_{10}\text{TiCoO}_{19}$ prepared by mixed oxide method

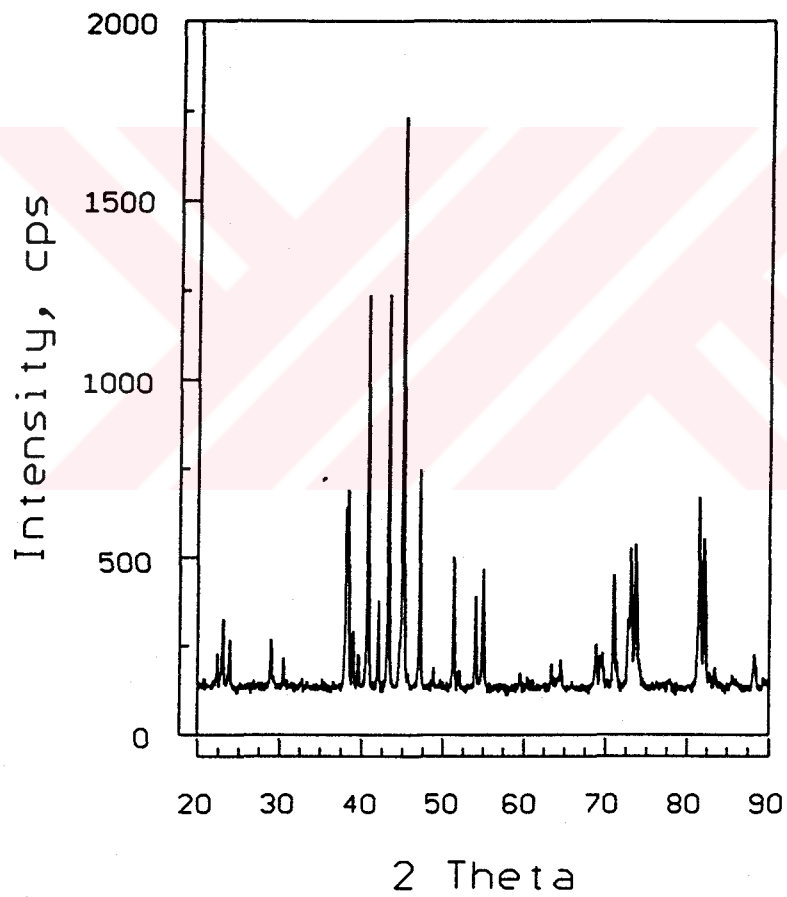


Figure 4.19. XRD diagram of $\text{BaFe}_9\text{Ti}_{1.5}\text{Co}_{1.5}\text{O}_{19}$ prepared by mixed oxide method

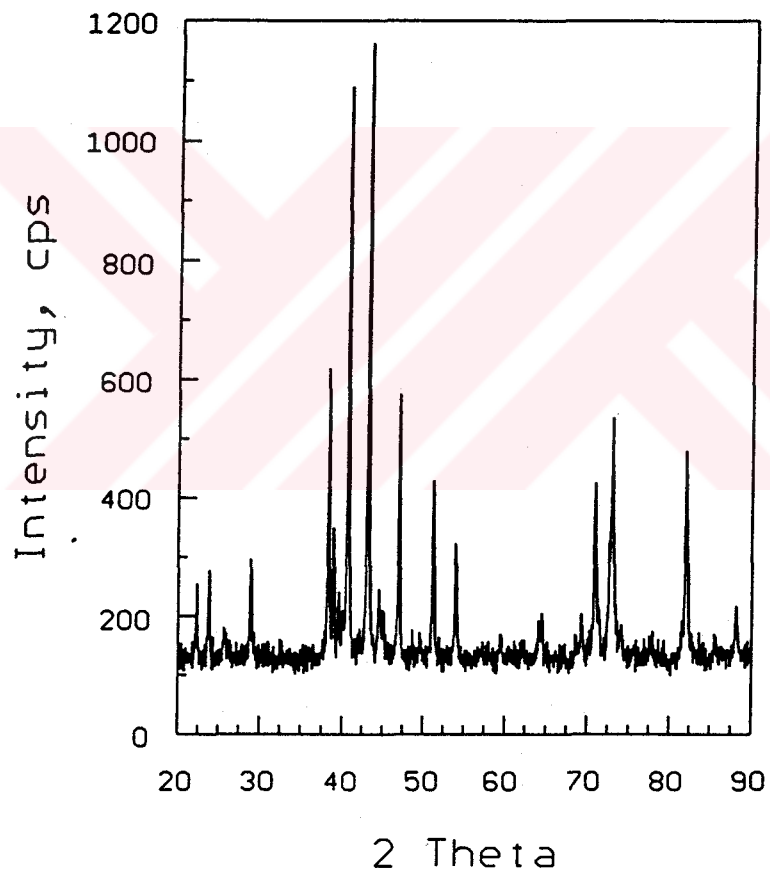


Figure 4.20. XRD diagram of $\text{BaFe}_{11.5}\text{Ti}_{0.5}\text{O}_{19}$ prepared by chemical precipitation technique.

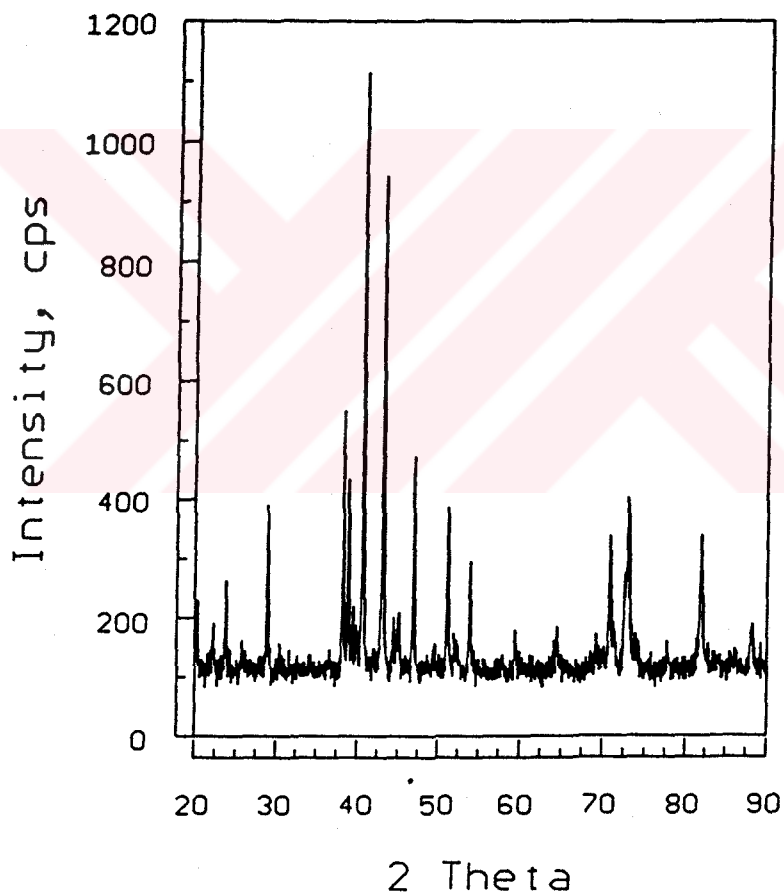


Figure 4.21. XRD diagram of $\text{BaFe}_{11}\text{TiO}_{19}$ prepared by chemical precipitation technique.

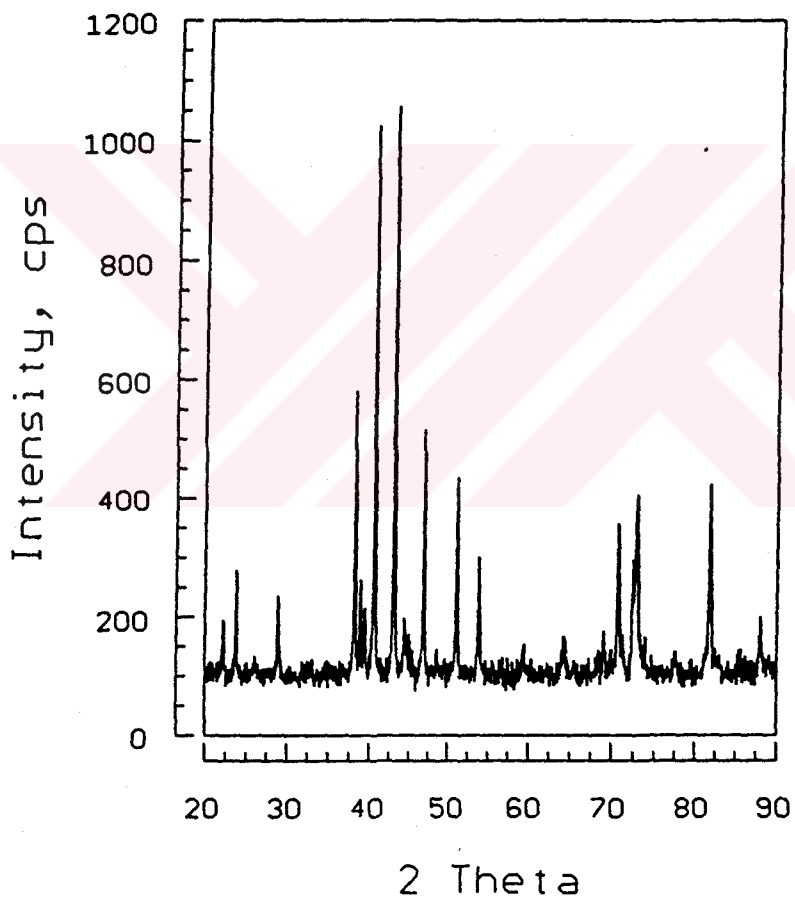


Figure 4.22. XRD diagram of BaFe_{10.5}Ti_{1.5}O₁₉ prepared by chemical precipitation technique.

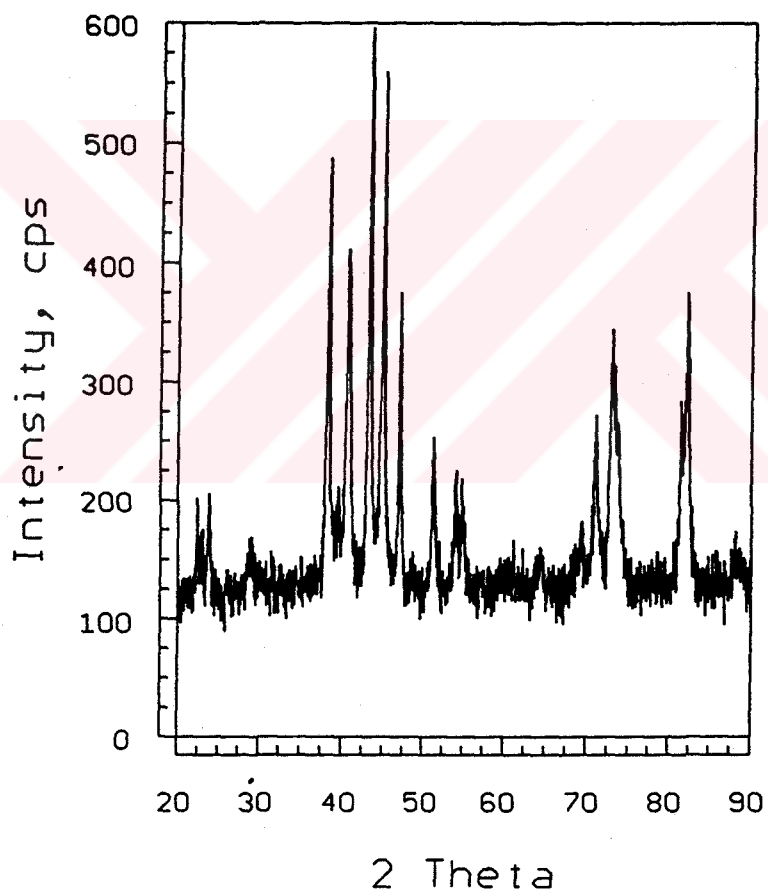


Figure 4.23. XRD diagram of $\text{BaFe}_{11.5}\text{Co}_{0.5}\text{O}_{19}$ prepared by chemical precipitation technique.

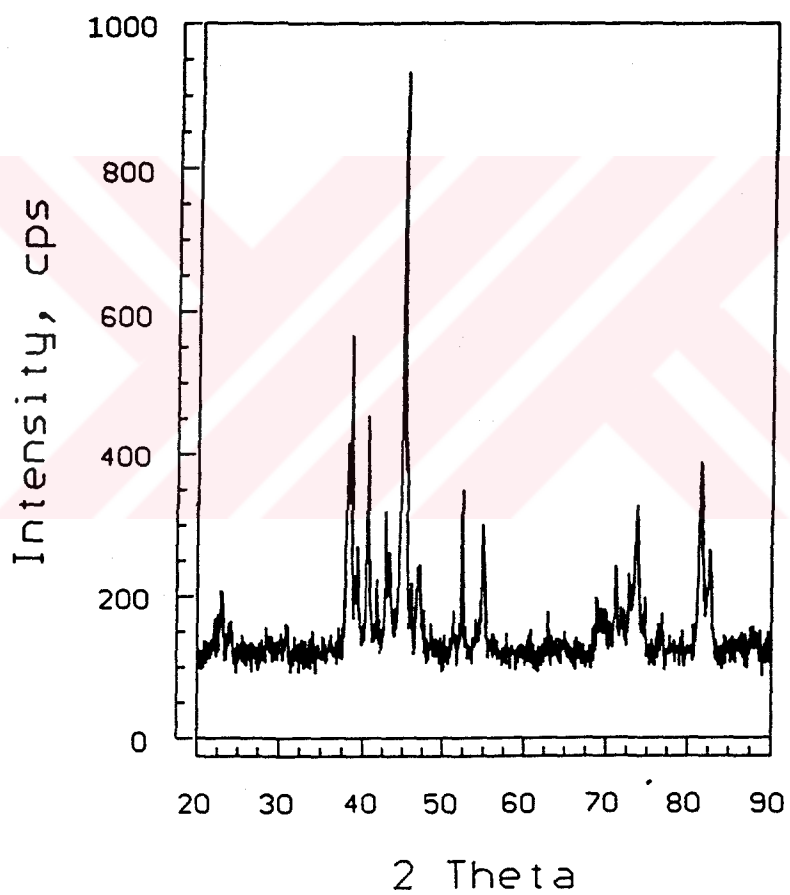


Figure 4.24. XRD diagram of $\text{BaFe}_{11}\text{CoO}_{19}$ prepared by chemical precipitation technique.

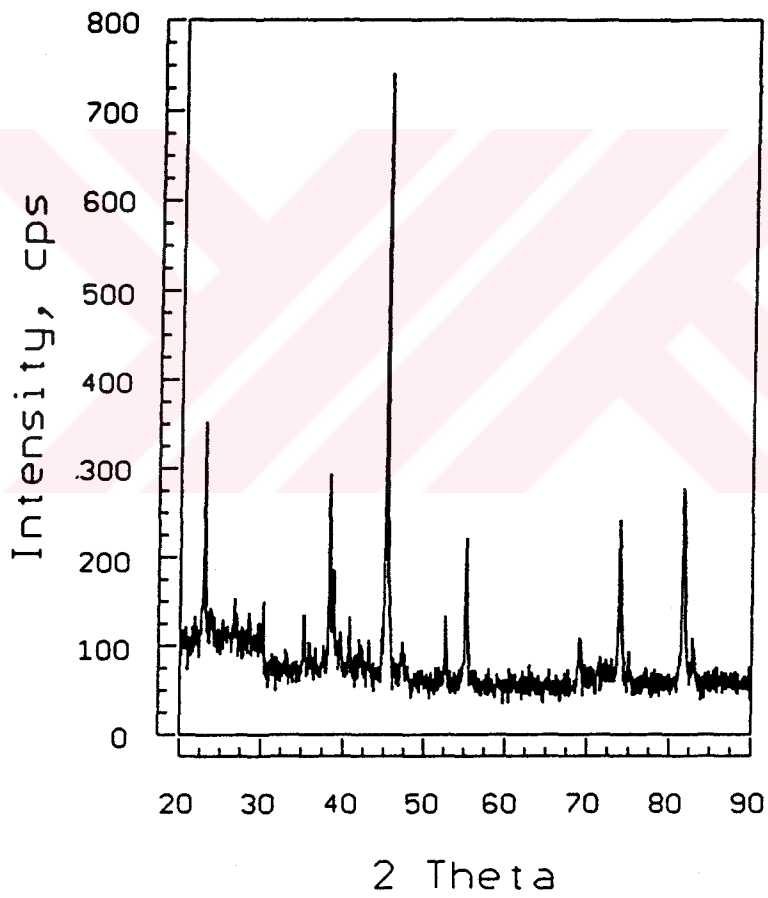


Figure 4.25. XRD diagram of BaFe_{10.5}Co_{1.5}O₁₉ prepared by chemical precipitation technique.

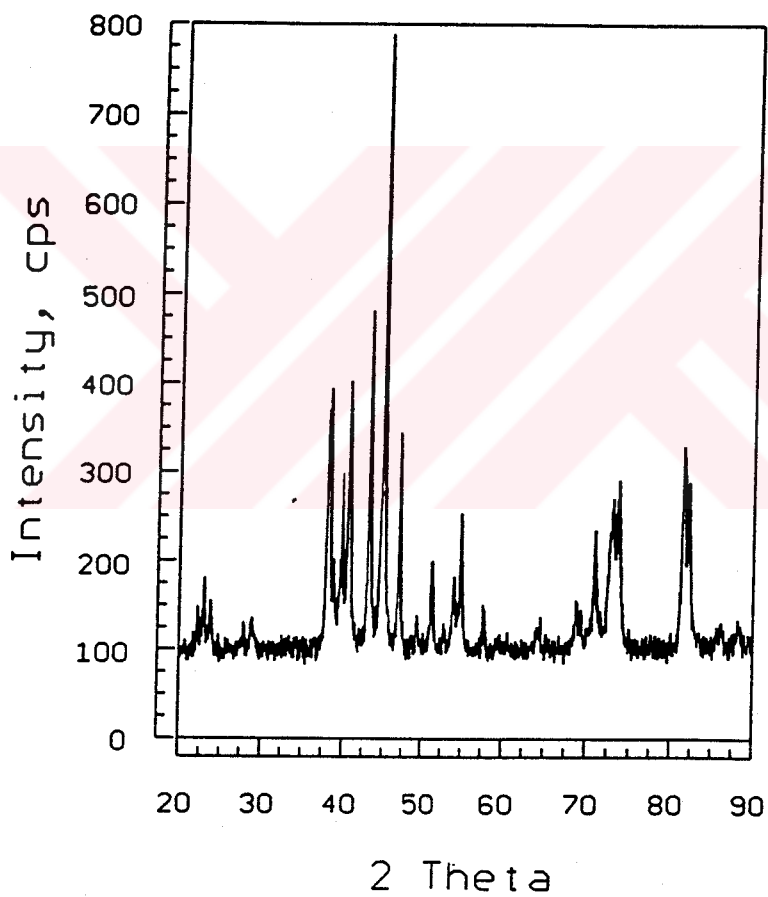


Figure 4.26. XRD diagram of $\text{BaFe}_{11}\text{Ti}_{0.5}\text{Co}_{0.5}\text{O}_{19}$ prepared by chemical precipitation technique.

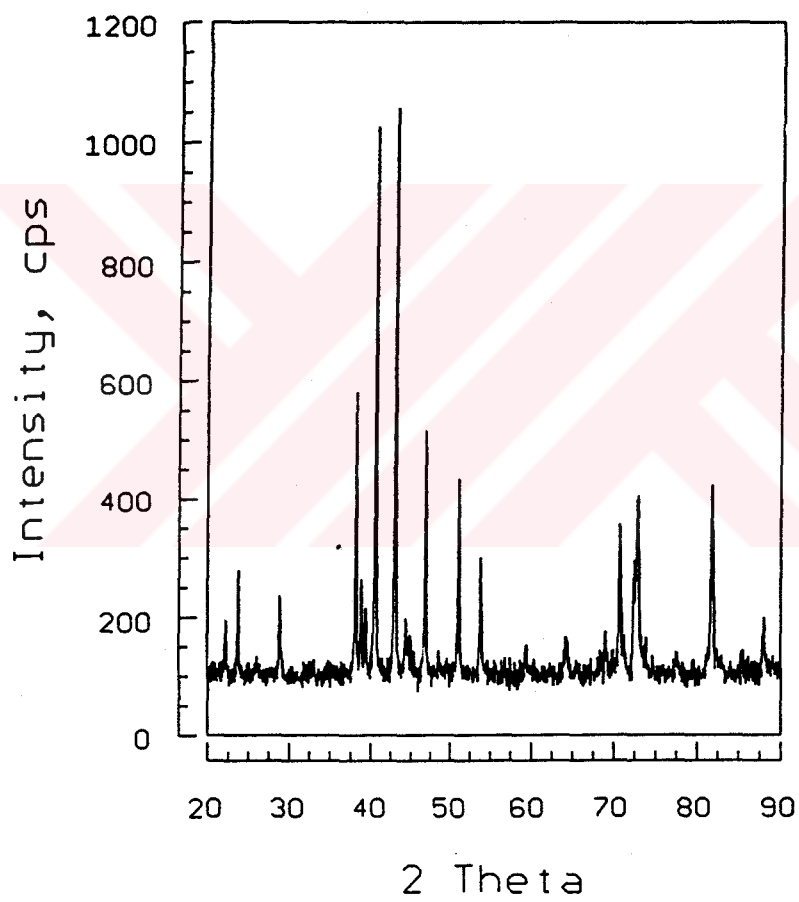


Figure 4.27. XRD diagram of BaFe₁₀TiCoO₁₉ prepared by chemical precipitation technique.

4.3. Dielectric and Magnetic Measurements

The reflection and transmission coefficients of the barium ferrites produced by the co-precipitation technique are given in Tables 4.5 through 4.13. These measurements were confined to the frequency range 8.5 to 12.5 GHz. The relative complex dielectric permittivity ϵ_r and the relative complex magnetic permeability μ_r could be deduced from the measured coefficients S_{11} and S_{21} by means of the analytical procedure described by W. B. Weir [27]. This procedure can be summarized as follows:

The propagation factor for a wave propagating through the dielectric material is defined as:

$$P = e^{-\gamma l} = e^{-(\alpha+j\beta)l} \dots\dots\dots(4-1)$$

where the terms are,

γ = propagation constant = $\alpha+j\beta$

α = attenuation constant

β = phase constant

l = length of the dielectric filled in the waveguide segment.

The propagation factor P could be related to the reflection and transmission coefficients by the equation:

$$P = [(S_{11})^2 - (S_{21})^2 - \Gamma] / [1 - (S_{11} - S_{21})\Gamma]$$

in which, the term Γ was defined through the following expressions:

$$\Gamma = \chi \pm (\chi^2 - 1)^{1/2}$$

where

$$\chi = [(S_{11})^2 - (S_{21})^2 + 1] / (2S_{11})$$

The complex dielectric permittivity and complex magnetic permeability were calculated by the help of the following expressions :

$$\frac{1}{\Lambda^2} = \frac{\epsilon_r \mu_r}{\lambda_0^2} - \frac{1}{\lambda_c^2} = - \left[\frac{1}{2\pi l} \ln \left(\frac{1}{P} \right) \right]^2 \dots\dots\dots(4-2)$$

and

$$\mu_r = \frac{1 + \Gamma}{\Lambda (1 - \Gamma) [1/\lambda_0^2 - 1/\lambda_c^2]^{1/2}} \dots\dots\dots(4-3)$$

where λ_0 is the wavelength in free space, and λ_c is the cut-off wavelength of the wave in the waveguide. The value of λ_0 was obtained at each frequency from the expression:

$$\lambda_0 = c / f_0$$

where c is the speed of light (3×10^8 m/sec) and f_0 is the frequency of the wave in Hz. The value of λ_c calculated from the length of the microwave segment was:

$$\lambda_c = 2 \times l = 2 \times 22.86 \text{ mm}$$

Equations (4-2) and (4-3) allowed to calculate the real and imaginary parts of the dielectric permittivity and magnetic permeability. These are related to the complex parameters by the following well-known expression:

$$\epsilon = \epsilon' - j \epsilon'' = \epsilon_r \epsilon_0 \dots\dots\dots(4-4)$$

where ϵ' and ϵ'' represent, respectively, the real and the imaginary parts of the complex dielectric permittivity. ϵ_r is the relative dielectric constant, and ϵ_0 is the permittivity of free space. The dielectric loss tangent, $\tan\delta_\epsilon$, was obtained from:

$$\tan\delta_\epsilon = \epsilon'' / \epsilon' \dots\dots\dots(4-5)$$

Similar expression could be written for the complex magnetic permeability, as follows:

$$\mu = \mu' - j\mu'' = \mu_r\mu_0 \dots\dots\dots(4-6)$$

$$\tan\delta_\mu = \mu'' / \mu' \dots\dots\dots(4-7)$$

The extent of absorption of the microwave by the ferrite medium could be ascertained from the magnitude of the attenuation constant α . This parameter is related to the frequency and the dielectric and magnetic parameters with the following equation, in nepers per length:

$$\alpha = 2\pi f \sqrt{\mu_0 \epsilon_0} \sqrt{(\mu_r' \epsilon_r' / 2)} [(\tan\delta_\mu \tan\delta_\epsilon - 1) + \{ 1 + \tan^2\delta_\mu \tan^2\delta_\epsilon + \tan^2\delta_\mu + \tan^2\delta_\epsilon \}^{0.5}]^{0.5} \dots\dots\dots(4-8)$$

The real and imaginary parts of the complex dielectric permittivity and complex magnetic permeability, together with the corresponding loss tangents are listed in Tables 4.5 to 4.13. The attenuation constants calculated from these are given in the last columns of the tables.

The absorption characteristics of the ferrites are described graphically in Figures 4.28 through 4.36. The curves in these figures were constructed from the attenuation results given in the above tables.

Figure 4.28 shows that the electromagnetic absorption of pure barium ferrite remained at a constant level of about 600 dB/mm throughout the entire frequency spectrum of the present study. Figure 4.29 to 4.36 show that, within the same frequency range, the absorption characteristics remained essentially unchanged by cobalt addition. Titanium additions caused lesser absorbance particularly at frequencies above 11 GHz. The absorbance obtained from combined cobalt and titanium, (Ti, Co=0.5 and Ti, Co=1.0) substitution was similar to that of pure barium ferrite.

When the reflection coefficients listed in these tables are examined, within the frequency range where the measurements were made, the reflection coefficients S_{11} remained at fairly low values. Thus with the exception of a few fluctuations the reflection characteristics of the powders remained more or less unchanged regardless of powder composition. In contrast to this, the coefficient S_{21} showed considerable deviation with the frequency of the wave and with powder composition.

The loss tangents $\tan\delta\epsilon$ and $\tan\delta\mu$ remained close to each other at many of the wave frequencies indicating that the wave entered the ferrite sample fully, with little reflection. This observation supports the low S_{11} values. The attenuation factors of various barium ferrites prepared in this study are displayed graphically in Figures 4.28 to 4.36. The curve in Figure 4.28 shows the absorption characteristics of pure barium ferrite. For a good part of the frequency interval, the absorbance remains constant with frequency. A jump at 9 GHz shows that a higher absorbance occurs at this frequency. It should be noted that the transmittance of the powder was also high at this particular frequency (Table 4.5).

Figures 4.29 to 4.31 display the effects of cobalt substitution. It is clear that cobalt additions do not cause much of a change in microwave absorption characteristics of the otherwise pure ferrite. Hence average α

values like 600 dB/mm are maintained across the frequency range covered. Although titanium showed similar effects at low frequencies there was dramatic decline in the absorption capability at frequencies around 11 to 11.5 GHz as could be seen in Figures 4.32 to 4.34.

The powders containing simultaneous cobalt and titanium doping exhibited features similar to pure barium ferrite. The sample doped with 0.5 TiO₂ and 0.5 CoO had a loss of attenuation above 12 GHz, other than that the attenuation characteristics remained almost unchanged.



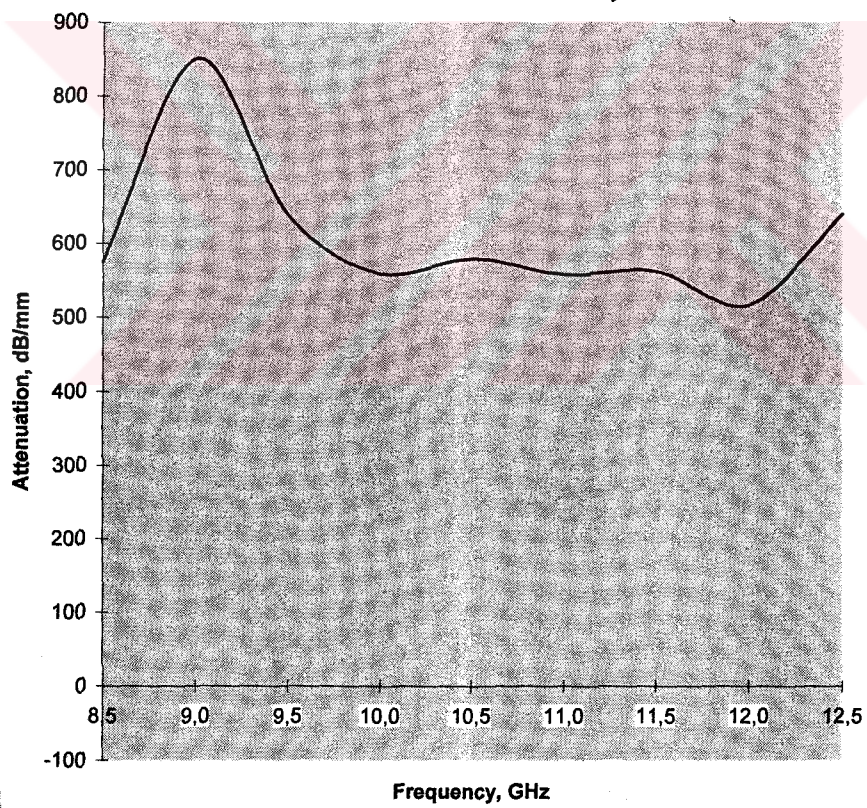


Figure 4.28. Absorption characteristics of $\text{BaFe}_{12}\text{O}_{19}$ (Sample No: 5).

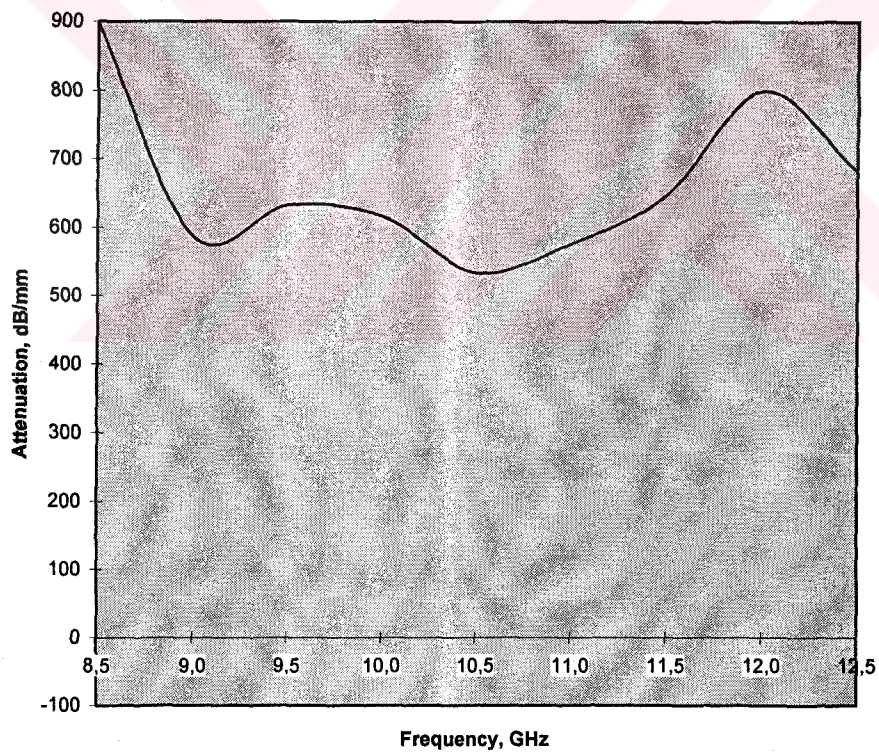


Figure 4.29. Absorption characteristics of BaFe_{11.5}Co_{0.5}O₁₉ (Sample No:6)

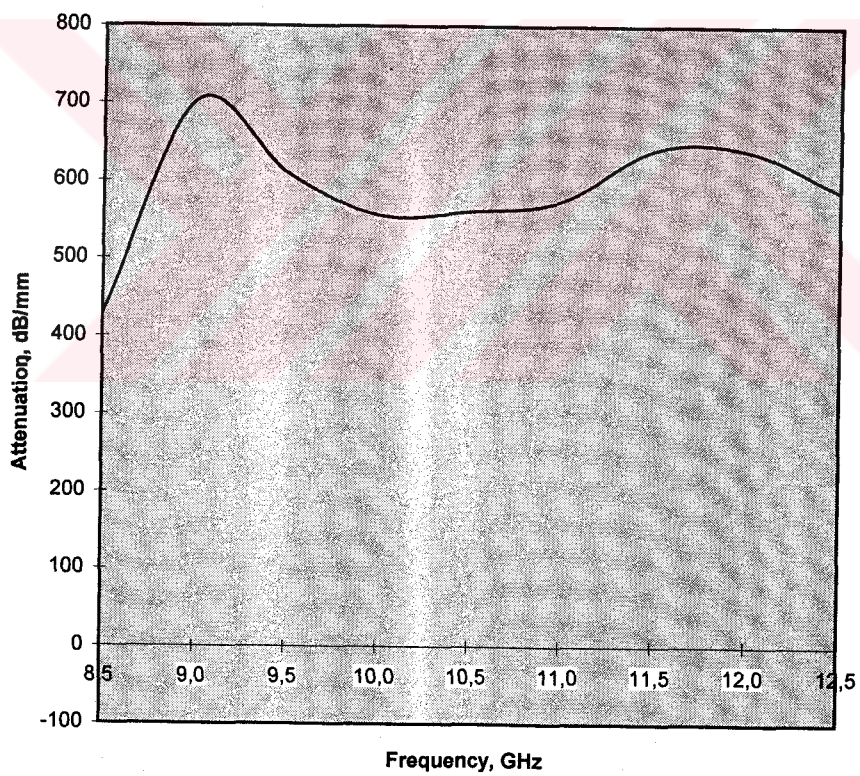


Figure 4.30. Absorption characteristics of BaFe₁₁CoO₁₉ (Sample No: 7).

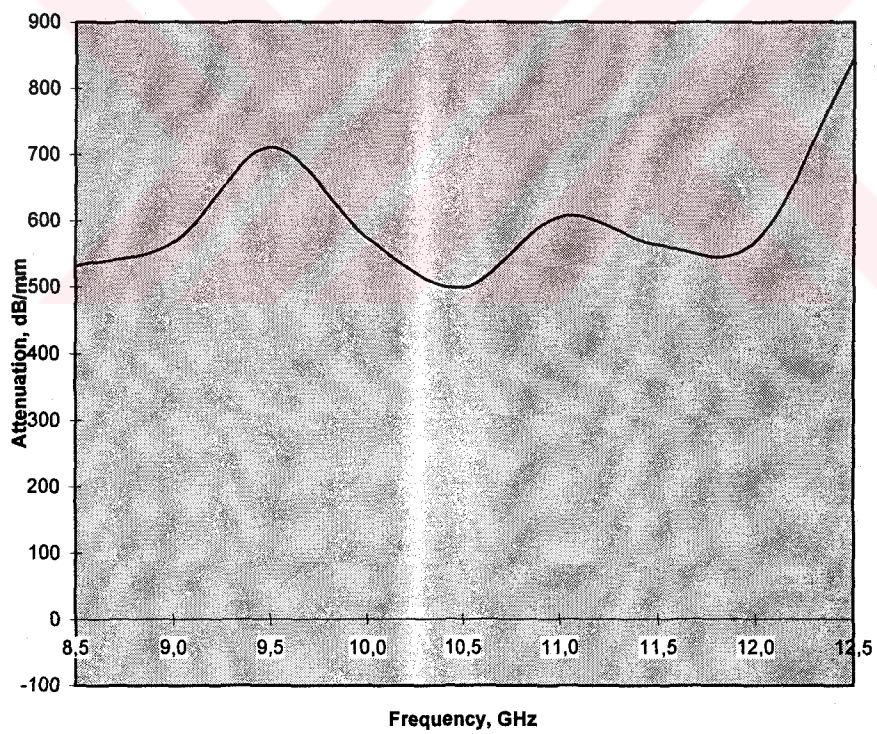


Figure 4.31. Absorption characteristics of BaFe_{10.5}Co_{1.5}O₁₉(Sample No: 8).

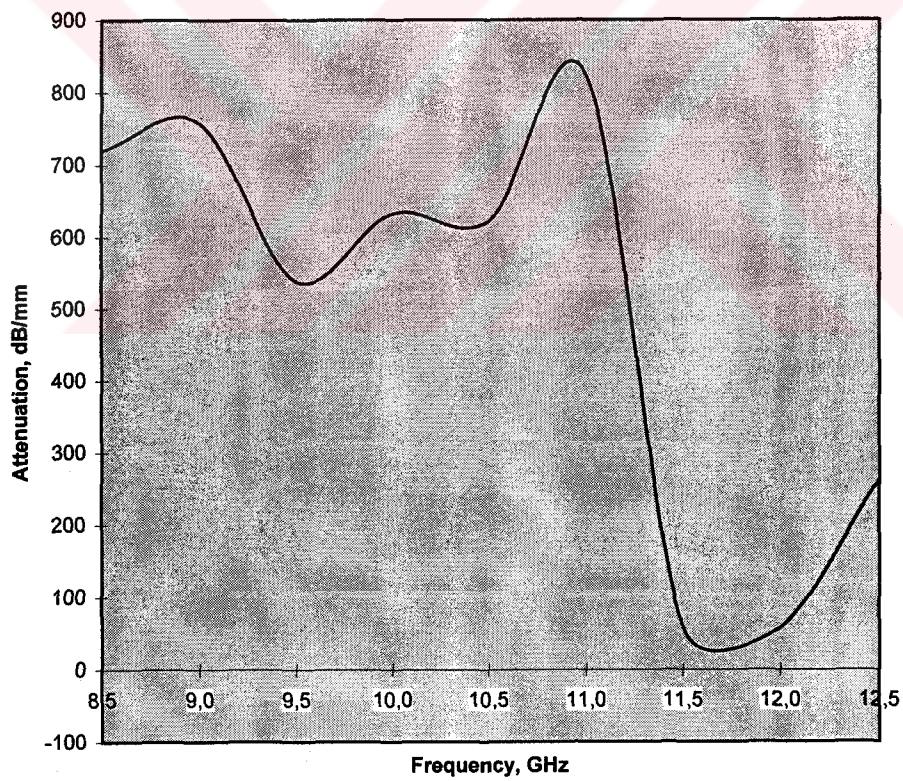


Figure 4.32. Absorption characteristics of BaFe_{11.5}Ti_{0.5}O₁₉ (Sample No: 9).

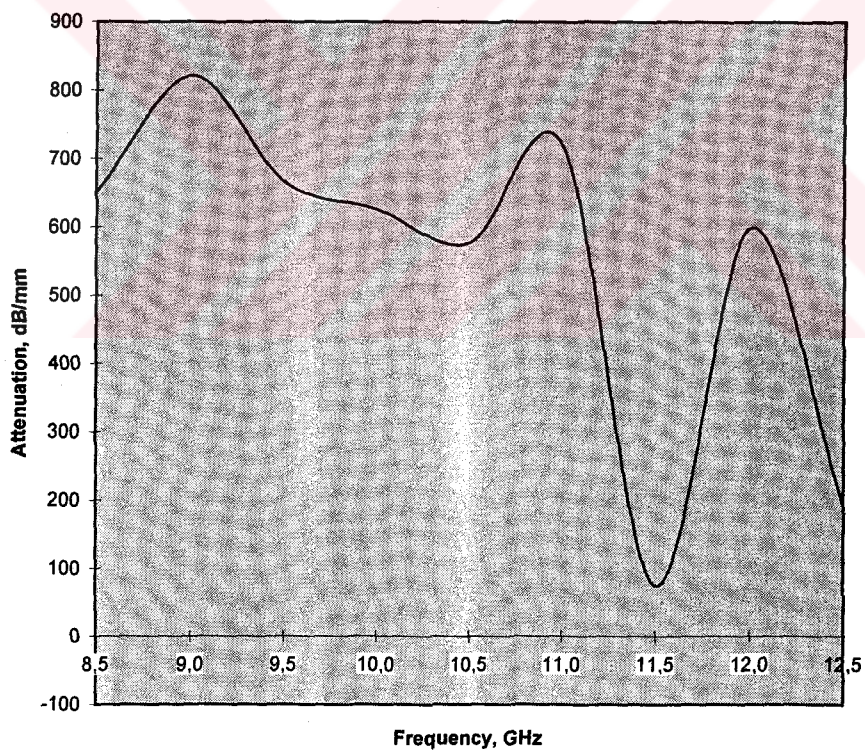


Figure 4.33. Absorption characteristics of BaFe₁₁TiO₁₉ (Sample No: 10).

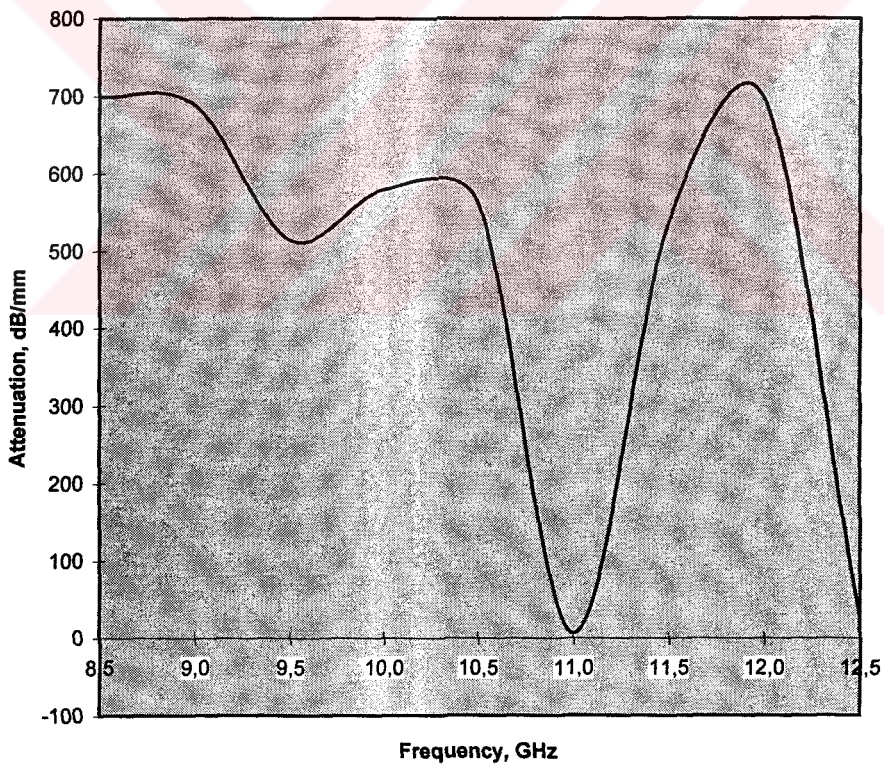


Figure 4.34. Absorption characteristics of BaFe_{10.5}Ti_{1.5}O₁₉ (Sample No:11)

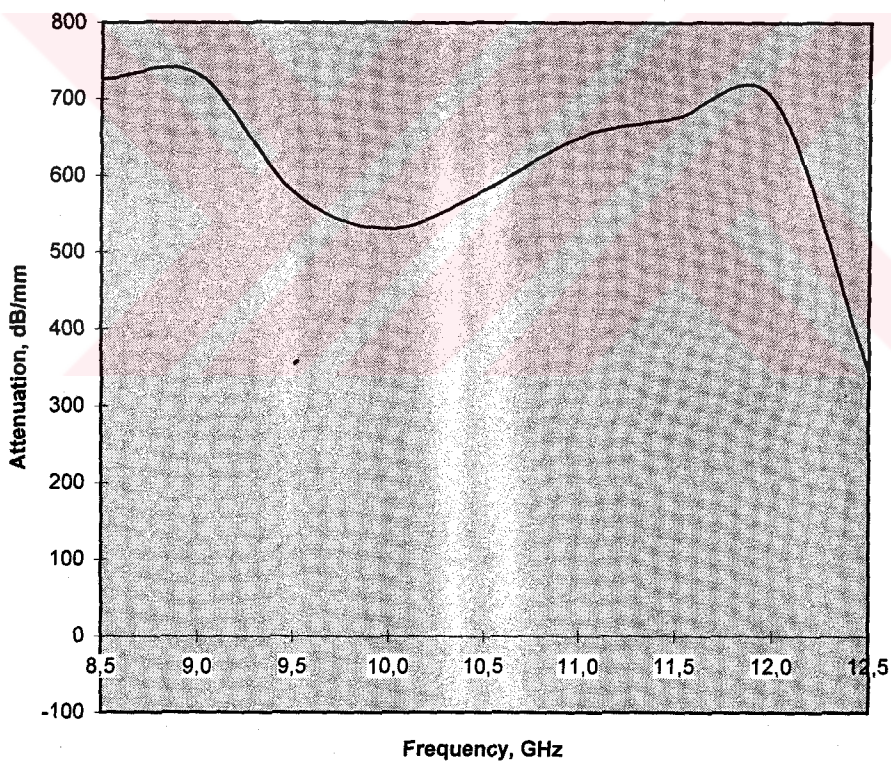


Figure 4.35. Absorption characteristics of BaFe₁₁Ti_{0.5}Co_{0.5}O₁₉
(Sample No:12)

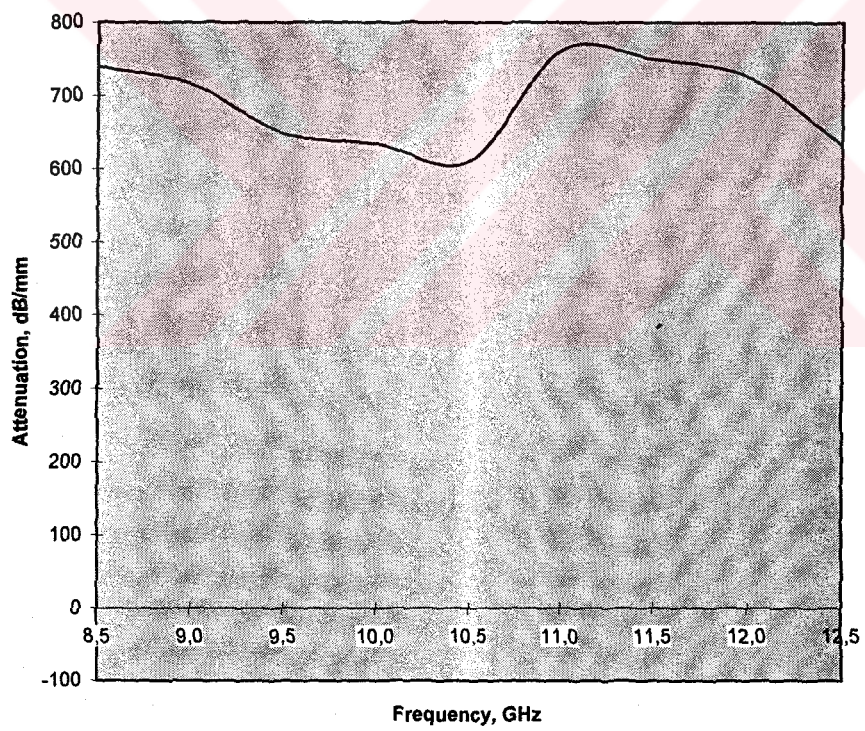


Figure 4.36. Absorption characteristics of BaFe₁₁TiCoO₁₉ (Sample No: 13).

Table 4.5 Dielectric and magnetic characteristics of BaFe₁₂O₁₉ (Sample No: 5)

Frequency GHz	S ₁₁ (dB)	S ₂₁ (dB)	Γ	Permeability		Permittivity		Loss Tangent tan ^δ	Attenuation α
				(re)	(im)	(re)	(im)		
8,5	-2	-3,5	0,67	1,49	-2,07	-4,88	4,97	-1,40	574,73
9,0	-3	-10,5	0,30	2,92	-3,09	-4,42	6,51	-1,06	849,92
9,5	-2,5	-3,4	0,68	-1,16	-1,91	4,87	5,29	1,65	638,24
10,0	-3,1	-4,4	0,60	-0,71	-1,89	2,36	3,70	2,67	558,53
10,5	-2,7	-4,8	0,58	-1,09	-1,60	3,77	4,30	1,47	578,69
11,0	-3	-1,4	0,85	-0,71	-1,63	1,84	3,58	2,31	557,26
11,5	-3,2	-1,4	0,85	0,20	-1,62	-0,89	3,34	-8,23	561,77
12,0	-2,8	-2,2	0,78	0,51	-1,22	-3,31	3,26	-2,41	516,79
12,5	-3,1	-5,3	0,54	0,55	-1,42	-3,19	4,09	-2,56	639,65

Table 4.6 Dielectric and magnetic characteristics of BaFe_{11,5}Co_{0,5}O₁₉ (Sample No: 6)

Frequency GHz	S ₁₁ (dB)	S ₂₁ (dB)	Γ	Permeability (re) (im)	Permittivity (re) (im)	Loss Tangent tan δ	Attenuation α
8,5	-2,3	-7,4	0,43	2,77 -3,11	-6,01 8,16	-1,12	898,77
9,0	-2,5	-6,4	0,48	-0,83 -2,15	3,11 4,41	2,61	586,88
9,5	-2,2	-8,1	0,39	-0,67 -1,98	2,81 5,07	2,93	632,72
10,0	-3,4	-8	0,40	-1,25 -2,06	2,94 4,19	1,65	616,02
10,5	-3,4	-2,4	0,76	-0,75 -1,76	2,00 3,33	2,35	533,99
11,0	-3,4	-2,3	0,77	-0,65 -1,78	1,42 3,52	2,74	576,47
11,5	-3,4	-5,4	0,54	0,12 -1,87	-0,79 3,85	-15,23	647,05
12,0	-3,7	-17	0,14	-1,47 -2,00	2,73 5,03	1,36	799,76
12,5	-4,1	-10,8	0,29	-1,71 -1,65	3,41 4,09	0,96	682,28

Table 4.7 Dielectric and magnetic characteristics of BaFe₁₁CoO₁₉ (Sample No: 7)

Frequency GHz	S ₁₁ (dB)	S ₂₁ (dB)	Γ	Permeability		Permittivity		Loss Tangent tan ^δ	Attenuation αc
				(re)	(im)	(re)	(im)		
8,5	-3	-6,5	0,47	2,44	2,08	-5,30	-2,66	0,85	429,22
9,0	-3,3	-15,9	0,16	-0,76	-2,85	2,28	4,82	3,76	702,50
9,5	-3,1	-8,7	0,37	-0,70	-2,18	2,90	4,19	3,13	609,79
10,0	-4	-6,4	0,48	-0,72	-2,10	2,02	3,31	2,91	555,95
10,5	-4,1	-6,7	0,46	-0,73	-1,96	1,99	3,28	2,67	560,59
11,0	-4,6	-4,7	0,58	-0,40	-2,00	0,91	3,10	5,02	574,28
11,5	-4,5	-5,5	0,53	0,39	-2,05	-0,75	3,45	-5,21	640,91
12,0	-4,6	-13	0,22	1,02	-1,82	-2,21	3,56	-1,77	640,05
12,5	-5	-9,6	0,33	-1,19	-1,62	2,36	3,11	1,37	587,36

Table 4.8 Dielectric and magnetic characteristics of BaFe_{10,5}Co_{1,5}O₁₉ (Sample No: 8)

Frequency GHz	S ₁₁ (dB)	S ₂₁ (dB)	Γ	Permeability (re) (im)	Permittivity (re) (im)	Loss Tangent tan δ	Attenuation α
8,5	-3	-4	0,63	2,32 -2,29	-4,40 3,88	-0,99	531,25
9,0	-3,6	-6	0,50	-0,99 -2,49	2,24 3,60	2,52	566,91
9,5	-3,4	-4,6	0,59	3,21 -2,28	-7,02 5,59	-0,71	710,56
10,0	-3,8	-6,1	0,50	-1,30 -2,00	3,17 3,72	1,53	573,05
10,5	-3,6	-2,3	0,77	-0,92 -1,66	2,48 3,05	1,80	498,49
11,0	-3,6	-2,5	0,75	-0,42 -1,92	0,80 3,59	4,56	605,87
11,5	-4	-3,4	0,68	0,13 -1,76	-0,74 3,07	-14,04	562,66
12,0	-3,7	-7,1	0,44	0,54 -1,54	-2,25 3,25	-2,85	568,92
12,5	-3,8	-13	0,22	-1,91 -1,92	3,85 5,37	1,01	846,51

Table 4.9 Dielectric and magnetic characteristics of BaFe_{11.5}Ti_{0.5}O₁₉ (Sample No: 9)

Frequency GHz	S ₁₁ (dB)	S ₂₁ (dB)	Γ	Permeability		Permittivity		Loss Tangent tan δ'	Loss Tangent tan δ	Attenuation α
				(re)	(im)	(re)	(im)			
8,5	-1,45	-5,95	0,50	1,43	-2,22	-5,00	7,35	-1,56	-1,47	719,81
9,0	-1,3	-4,8	0,58	1,50	-1,78	-8,03	9,07	-1,19	-1,13	757,97
9,5	-2	-1,8	0,81	-0,97	-1,59	4,23	4,53	1,63	1,07	538,46
10,0	-1,9	-2	0,79	-0,84	-1,71	2,99	5,31	2,04	1,78	632,58
10,5	-2,1	-2,55	0,75	-0,99	-1,60	3,31	5,00	1,61	1,51	621,68
11,0	-1,8	-2,7	0,73	-0,77	-1,92	1,74	6,62	2,49	3,80	822,74
11,5	-1,8	-3,3	0,68	-0,31	-1,55	-0,16	5,06	4,95	-32,07	57,12
12,0	-2,01	-7,6	0,42	-0,17	-1,32	-1,31	3,84	7,85	-2,94	58,66
12,5	-2,35	-2,75	0,73	-0,46	0,57	2,92	-1,59	-1,25	-0,54	262,88

Table 4.10 Dielectric and magnetic characteristics of BaFe₁₁TiO₁₉ (Sample No: 10)

Frequency GHz	S ₁₁ (dB)	S ₂₁ (dB)	Γ	Permeability		Permittivity		Loss Tangent tan δ	Attenuation α
				(re)	(im)	(re)	(im)		
8,5	-1,45	-11,05	0,28	-0,58	-2,12	3,31	6,19	3,68	1,87
9,0	-1,6	-9,1	0,35	1,37	-2,18	-5,29	8,70	-1,59	-1,64
9,5	-1,9	-7,1	0,44	-0,99	-1,88	3,85	5,95	1,90	1,54
10,0	-1,9	-3,3	0,68	-1,10	-1,63	4,16	5,48	1,48	1,32
10,5	-2,5	-1,5	0,84	-0,93	-1,65	2,56	4,16	1,77	1,63
11,0	-2,2	-1,9	0,80	-0,56	-1,86	1,07	5,23	3,33	4,91
11,5	-2,2	-8,5	0,38	-0,06	-1,55	-1,23	4,45	26,97	-3,60
12,0	-2,8	-9,8	0,32	0,25	-1,43	-2,50	3,76	-5,72	-1,51
12,5	-3,05	-4,55	0,59	-1,26	0,54	4,03	-0,91	-0,43	-0,23

Table 4.11 Dielectric and magnetic characteristics of BaFe_{10,5}Ti_{1,5}O₁₉ (Sample No: 11).

Frequency GHz	S ₁₁ (dB)	S ₂₁ (dB)	Γ	Permeability (re)	(im)	Permittivity (re)	(im)	Loss Tangent tan δ	tan ε	Attenuation α
8,5	-2,1	-3,4	0,68	-1,48	-2,39	5,36	6,41	1,61	1,20	699,63
9,0	-2	-3,2	0,69	-1,57	-2,00	6,28	6,66	1,28	1,06	688,99
9,5	-2,2	-1,5	0,84	-0,84	-1,60	3,96	4,04	1,90	1,02	514,22
10,0	-2,6	-4,1	0,62	-1,06	-1,75	3,35	4,34	1,66	1,30	579,32
10,5	-2,6	-0,7	0,92	-0,65	-1,68	1,96	3,90	2,59	1,99	562,88
11,0	-2,7	-2,5	0,75	-0,13	-1,85	-0,23	4,28	13,79	-18,73	6,20
11,5	-2,9	-2,9	0,72	0,52	-1,36	-3,37	3,43	-2,64	-1,02	536,85
12,0	-3,1	-14	0,20	0,37	-1,69	-2,15	4,47	-4,53	-2,08	697,26
12,5	-3,5	-1,6	0,83	-1,64	-0,03	5,20	0,23	0,02	0,04	23,71

Table 4.12 Dielectric and magnetic characteristics of BaFe₁₁Ti_{0.5}Co_{0.5}O₁₉ (Sample No: 12)

Frequency GHz	S ₁₁ (dB)	S ₂₁ (dB)	Γ	Permeability		Permittivity		Loss Tangent tan δ	Attenuation α _c
				(re)	(im)	(re)	(im)		
8,5	-2,8	-8,2	0,39	2,52	-2,89	-4,74	5,76	-1,14	726,01
9,0	-2,6	-7,6	0,42	-1,59	-2,48	4,30	6,09	1,55	732,48
9,5	-2,5	-4,5	0,60	-1,24	-1,83	4,16	4,58	1,48	579,01
10,0	-3,3	-2,8	0,72	-1,06	-1,84	2,56	3,47	1,73	530,33
10,5	-3,6	-2,5	0,75	-0,64	-1,98	1,23	3,52	3,11	580,65
11,0	-3,6	-8,1	0,39	0,33	-2,02	-1,19	3,92	-6,12	650,19
11,5	-4,1	-21	0,09	0,57	-1,98	-1,90	3,93	-3,46	675,77
12,0	-4,6	-10,8	0,29	-2,40	-1,80	4,26	4,27	0,75	700,87
12,5	-4,8	-5,7	0,52	-1,97	-0,86	3,79	1,99	0,44	343,57

Table 4.13 Dielectric and magnetic characteristics of BaFe₁₀TiCoO₁₉ (Sample No: 13)

Frequency GHz	IS111 (dB)	IS211 (dB)	Γ	Permeability		Permittivity		Loss Tangent		Attenuation α
				(re)	(im)	(re)	(im)	tan δ	tan ε	
8,5	-2,4	-13,2	0,22	-0,66	-2,99	2,20	5,74	4,52	2,61	740,18
9,0	-2,6	-14,9	0,18	-0,52	-2,69	1,89	5,34	5,13	2,83	716,39
9,5	-2,8	-13,7	0,21	-0,48	-2,28	2,01	4,59	4,81	2,29	648,29
10,0	-3,1	-8,3	0,38	-0,60	-2,13	1,87	4,27	3,54	2,29	634,18
10,5	-3,3	-4,2	0,62	-0,26	-2,01	1,03	3,81	7,77	3,70	610,30
11,0	-3,1	-6,4	0,48	0,58	-2,20	-1,18	4,97	-3,76	-4,20	762,14
11,5	-3,2	-12,6	0,23	0,74	-1,98	-1,77	4,88	-2,69	-2,76	749,95
12,0	-3,5	-15,8	0,16	-0,90	-1,85	2,11	4,52	2,06	2,15	726,05
12,5	-3,7	-8,6	0,37	-1,14	-1,54	2,70	3,79	1,35	1,41	632,84

CHAPTER V

DISCUSSION AND CONCLUSIONS

The objective of the present thesis was to produce synthetic ferrite powders and to study their interaction with electromagnetic waves at microwave frequencies. The compositions of the ferrite powders were based on the nominal molecular formula of $\text{BaFe}_{12}\text{O}_{19}$. The particular concern with the wave interaction was in the absorption characteristics of the ferrite powders. The information generated could be used in designing and manufacturing radar absorbing materials for low visible aircraft applications.

Literature survey on methods of synthesizing barium ferrite powders revealed that the chemical routes involving coprecipitation from suitable salt solutions would be the preferred one for meeting the morphology requirements. Such powders would be thin and tiny platelets so that they would give mechanical alignment in the RAM layer formed when used as a paint like suspension with a liquid epoxy.

The strategy of making barium ferrite powders through chemical methods was applied by using aqueous chloride solutions of barium and iron. The precipitation was carried out under controlled pH-temperature conditions so that well defined stoichiometry could be maintained in the product. The co-precipitated powders were washed and then calcined properly to obtain the barium ferrites having morphological features required for RAM applications.

The barium ferrite powder particles produced by the co-precipitation technique were extremely fine and they were almost monosized. The particles were thin hexagonal platelets typical of those used in making the magnetic tapes for the recording media. The platelets were of sub-micron size, typically they measured 0.7 micron across the diagonal with a thickness 1/10 th of this dimension.

The chemical compositions of barium ferrite powders were modified by substituting part of the iron in the crystal structure with cobalt or titanium or both. Cobalt additions refined the powder even further when substitution level was kept at 0.5 mole CoO. Further additions brought back the morphology attained in the pure ferrite powder. Doping with titanium or with titanium plus cobalt did not produce significant changes in the powder morphology.

The examination of x-ray diffraction patterns revealed interesting variations in the crystallization behavior of the cobalt doped powders. As the cobalt substitution was increased gradually towards 1.5 mole level the diffraction from the 200 plane of the ferrite became predominant.

A simulated vector network analyzer available in the Electrical and Electronics Department of METU was used for the assessment of the dielectric and magnetic parameters of the ferrite powders. The parameters examined were those which determined largely the RAM characteristics of these powders. The circuit permitted to make measurements within the frequency interval 8.5 to 12.5 GHz of the microwave region.

The reflection coefficients of the pure and doped barium ferrites were quite low. Due to the scarcity of published information in the open literature, there is no chance for making a direct comparison of the data obtained in this study with the measurements of other investigators

working in this area. Perini and Cohen [2] reported the values for a 4 layer RAM of unspecified dielectric at microwave frequencies of 5 to 7 GHz; the reflectances given for this material were in the range 18 to 32 dB. Amin and James [3, 4] displayed their reflectance data taken in multilayer RAMs; the values for ferrite based absorbers having 3 and 5 layers were in the range 10 to 13 dB in the frequency interval of 8.5 to 12.5 GHz.

The reflection loss characteristics of the barium ferrite powders prepared in the present study are better than those reported in both of the papers quoted above as shown in Figure 5.1. Unfortunately, the attenuation characteristics obtained in the present thesis cannot be compared with any literature value since none has hitherto been published according to our knowledge. It should however be stressed that, in general the powders synthesized exhibited rather high attenuation, thus they should be ideal for RAM applications. The titanium doping caused a sharp decline in the absorption characteristics of the ferrite powder particularly at microwave frequencies of 10 to 11 GHz. This can be linked with the fact that the magneto-crystalline anisotropy energy of barium ferrite is reduced drastically in the presence of titanium. Thus, it may be concluded that titanium additions may be good for recording tape applications but it should be avoided in RAM intended barium ferrites.

The work reported in this thesis represents only a start of a more comprehensive study that should be planned on ceramics intended for use at microwave frequencies. The availability of a reliable measurement facility for the determination of magnetic permeability and dielectric permittivity is essential for this type of work. Hence future efforts should be directed towards establishing this reliability and then work can proceed towards manufacturing composite RAMs made by the use of outstanding ferrite powders developed in this thesis.

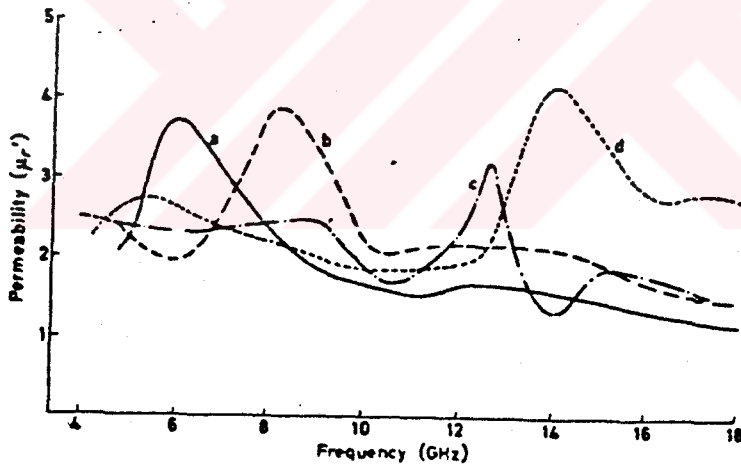
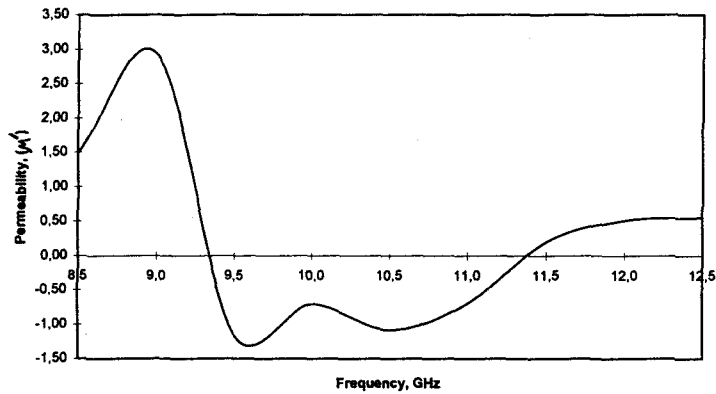


Figure 5.1 Reflection loss characteristics of the ferrite powders produced in the present study (sample 5) as compared with the reflectances quoted in literature (a, b, c and d in lower figure show barium ferrites with unknown amount of same dopants, cobalt and titanium) [3].

REFERENCES

- [1] Brown, A.S., 'Stealth Comes of Age', *Aerospace America*, pp 16-20, 36; March 1990
- [2] Perini, J. And Cohen, L.S.; 'Design of Broad-Band Radar-Absorbing Materials for Large Angles of Incidence', *IEEE Trans. Electromag. Comp.*, Vol. 35, No.2, pp 223-30, May 1993.
- [3] James, J.R. and Amin, M.B.; 'Techniques for Utilization of Hexagonal Ferrites in Radar Absorbers, Part I', *The Radio and Electronic Engineer*, Vol. 57, No.5, pp 209-18, May 1981.
- [4] James, J.R. and Amin, M.B.; 'Techniques for Utilization of Hexagonal Ferrites in Radar Absorbers, Part II', *The Radio and Electronic Engineer*, Vol. 57, No.5, pp 219-25, May 1981.
- [5] O'Connor, M. And Belson, H.J.; *J. Appl. Phys.* 41, 1028, 1970.
- [6] Moulson, A.J. and Herbert, J.M.; *Electroceramics : Materials, Properties, and Applications*, Chambridge Univ. Press, Chapter 9, 1990
- [7] Abraham, T.; 'Economics of Ceramic Magnets' *Am. Cer. Soc. Bull.* Vol. 73, No.8, pp 62-5, August 1994.
- [8] Bradley, F. N.; *Materials For Magnetic Functions*, Hayden Book Company, Inc., New York, 1971.
- [9] Hench, L.L. and West, J.K.; *Principles of Electronic Ceramics*, Chapter 7.
- [10] Abelslod, V.; *Ark. Kem. Min. Geol.* 12A(29), 1 1938.
- [11] Albanese, G.I.; *Phys. Collogue*, Cl, supply, 4, 38, C1-85, 1977.
- [12] Smit, J. And Wijn, H.P.J.; *Ferrites*, John Wiley & Sons Inc. New York, Chapter 2, 1959.

- [13] Kuester, E.F. and Holloway, C.L.; 'Improved Low-Frequency Performance of Pyramid-Cone Absorbers for Application in Semi-Anechoic Chambers', Proc. 1989 IEEE Int. Symp. EMC, Denver, CO, pp 394-8, 1989.
- [14] Hansen, D.; Ari, N. And Garbe, H.; 'An Investigation into the Scattering and Radiation Characteristic of RF-Absorber', Proc. 1988 IEEE Int. Symp. EMC, Seattle, pp 99-105, 1988.
- [15] Ari, N.; Hansen, D. And Garbe, H.; 'Analysis and Measurement of Electromagnetic Scattering by Pyramidal Absorbers' Proc. 1989, Zurich Int. Symp. Technology. Exhibition on EMC, Zurich, Switzerland, 1989
- [16] Wilson, P., Garbe, H. And Hansen, D.; 'A Simulation of the Site Attenuation in Anechoic Chambers : Try Before You Buy', Proc. 9th Int. Symp. Exh. On EMC, Zurich, Switzerland, pp 311-6, 1991.
- [17] Stuijts, A.L.; 'Sintering of Ceramic Permanent Magnetic Materials', British Cer. Soc. Trans., pp 57-74, 1955.
- [18] Roos, W.; 'Formation of Chemically Coprecipitated Barium Ferrite', J. Am. Cer. Soc., Vol. 63, No.11-12, pp 601-3, Nov.-Dec. 1980.
- [19] Lee, B.W. and Orr, K.K.; 'Filtering and Sintering of Ba-ferrite Using Co-precipitation of Hydroxides', Ceramic Trans., Ceramic Powder Science IV, Vol. 22, Eds. Hirano, S. And Messing, G.L.; The Am. Cer. Soc., pp 597-602, 1991.
- [20] Haneda, K., Miyakawa, C. And Kojima, H.; 'Preparation of High Coercivity BaFe₁₂O₁₉', J. Am. Cer. Soc., Vol. 57, No.8, pp 354-7, August 1974.
- [21] Broek van den, C.A.M. and Stuijts, A.L.; 'Philips Technical Review, Ferroxdure' Vol. 37, No.7, pp 156-77, 1977.
- [22] Johnson, D.W.Jr.; 'Nonconventional Powder Preparation Techniques', Cer. Bull., Vol. 60, No.2, pp 221-23, 1981.
- [23] Tenzer, R.K.; 'Influence of Particle Size on Coercive Force of Barium Ferrite Powders', J. Appl. Phys., Vol. 34, No.4-Pt.2, pp 1267-68, 1963.
- [24] Richter, H.G. and Dietrich, H.E.; 'Magnetic Properties of Fine Milled Barium and Strontium Ferrite', IEEE Trans. Magn., Vol. 4, No.3, pp 263-67, 1968.

- [25]** Haneda, K. and Kojima, H.; 'Effect of Milling on the Intrinsic Coercivity of Barium Ferrite Powders', J. Am. Cer. Soc., Vol. 57, No.2, pp 68-71, 1974.
- [26]** Ghodgaonkar, D.K.; Varadan, V.V. and Varadan, V.K.; 'Free-Space Measurement of Complex Permittivity and Complex Permeability of Magnetic Materials at Microwave Frequencies', IEEE Trans. Instr. And Meas. Vol. 39, No.2, pp 387-94, April 1990.
- [27]** Weir, W.B.; 'Automatic Measurement of Complex Dielectric Constant and Permeability at Microwave Frequencies', Proc. IEEE, Vol. 62, No.1, pp 33-6, January 1974.

